

Received: 10.01.2025

Accepted: 13.04.2025

Research Article

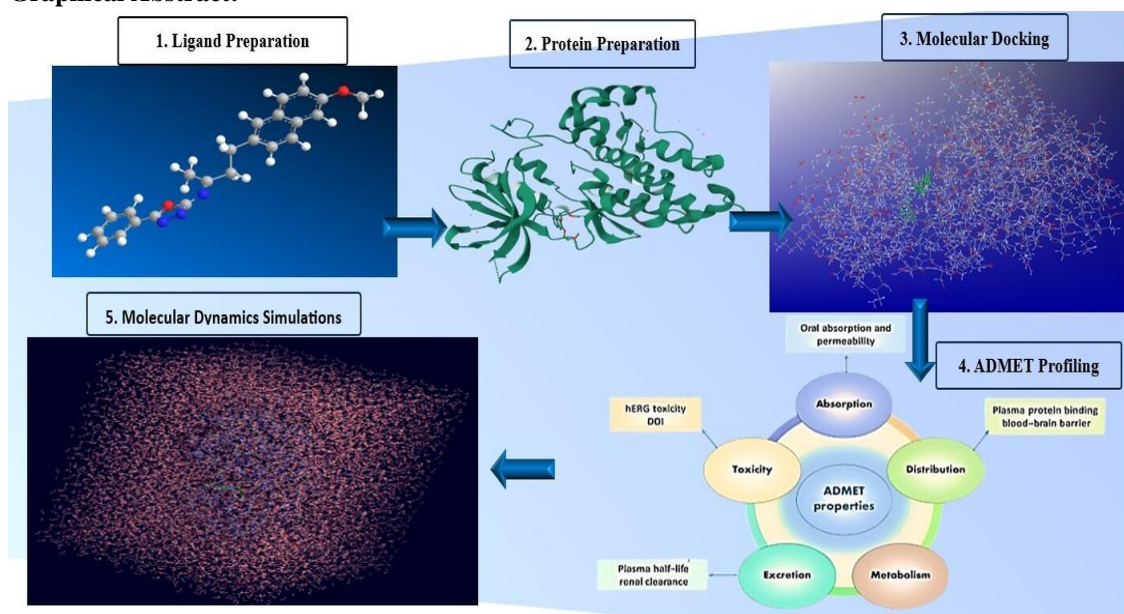
In Silico Design, Molecular Docking, Molecular Dynamics Simulations, and Pharmacokinetics Insights of Novel 1,3,4-Oxadiazole and 1,3,4-Thiadiazole Derivatives as Potential EGFR Inhibitors

Ahmed Haloob Kadhim^{a,1}, Monther Faisal Mahdi^a, Ayad MR Rauf^b

^aDepartment of Pharmaceutical Chemistry, College of Pharmacy, Mustansiriyah University, Baghdad, Iraq.

^bCollege of Pharmacy, Al-Farahidi University, Baghdad, Iraq.

Graphical Abstract:



Abstract: This study investigates novel 1,3,4-oxadiazole and 1,3,4-thiadiazole derivatives (A1–A6) that act as potential inhibitors of EGFR, a key target in non-small cell lung cancer (NSCLC). Using a comprehensive in silico approach, including molecular docking, molecular dynamics (MD) simulations, and ADMET profiling, the pharmacological potential of these compounds was evaluated. EGFR mutations, particularly the T790M gatekeeper mutation, drive resistance for first-generation tyrosine kinase inhibitors (TKIs) such as Erlotinib, highlighting the need for next-generation inhibitors.

All designed compounds complied with Lipinski's Rule of Five, and ADMET analysis confirmed favorable pharmacokinetics. Docking studies revealed stronger EGFR binding affinity than Erlotinib, with A1 and A2 showing PLP fitness scores of 90.61 and 83.77, respectively. Key interactions with residues THR830 and THR766 contributed to high stability. MD simulations over 100 ns confirmed structural and binding stability of the A1-EGFR complex through RMSD and RMSF analyses. A1 also demonstrated excellent pharmacokinetic potential (Caco-2: 2636.59 nm/sec; LogP: 4.19), indicating high permeability and lipophilicity. These findings position A1 as a strong candidate for experimental validation against EGFR-driven NSCLC.

¹ Corresponding Authors

e-mail: m.zakarianejad@yahoo.com & mzakarianejad@pnu.ac.ir

Highlights

- Novel 1,3,4-oxadiazole/thiadiazole (A1–A6) as potential EGFR inhibitors (in silico).
- A1 had the highest PLPfitness (90.61) from docking with strong binding affinity.
- ADMET profiles indicated promising PK, Lipinski compliance, and low cardiotoxicity.
- Molecular dynamics confirmed A1's stable binding in EGFR over 100-ns simulation.
- Integrated approach suggests these derivatives are promising for experimental validation.

Keywords: EGFR inhibitors, in silico drug design, Molecular docking, ADMET profiling, Molecular dynamics simulations.

1. Introduction

Lung cancer poses one of the most significant public health challenges worldwide, accounting for more than 2.2 million cases each year and about 1.8 million deaths.^[1] It accounts for more fatalities than breast, prostate, and colon cancers combined, highlighting its significant clinical and societal burden. Non-small cell lung cancer (NSCLC) constitutes the majority of lung cancer cases. (80–85%) and is often linked with genetic mutations.^[2] Among these, the epidermal growth factor receptor (EGFR) pathway plays a crucial role in tumor initiation, proliferation, and survival. EGFR overexpression or mutations, particularly in exons 19 and 21, have been identified in 40-89% of NSCLC cases, making it a prime target for therapeutic intervention.^[1,3]

Protein tyrosine kinases (PTKs) are vital enzymes that govern numerous functions by phosphorylating tyrosine residues within target proteins. Abnormalities in tyrosine kinase activity can lead to dysregulated cell growth, proliferation, and apoptosis, all of which play crucial roles in the progression of cancer.^[4,5]

The treatment of NSCLC has been significantly improved by first-generation epidermal growth factor receptor tyrosine kinase inhibitors (EGFR-TKIs), such as erlotinib^[6] and Gefitinib^[7]. These agents selectively target activating EGFR mutations, particularly exon 19 deletions and the L858R point mutation in exon 21, which are common in up to 50% of Asian patients and 10–20% of Caucasian patients, including non-smokers and females^[8,9]. However, resistance typically arises within 9–14 months, mainly due to the T790M gatekeeper mutation, which reduces drug binding.^[10]

Second-generation TKIs, including afatinib and dacomitinib, act as irreversible inhibitors of EGFR

that harbor mutations, such as L858R or exon 19 deletions-mutations often linked to resistance to first-generation agents^[11]. These inhibitors covalently bind to the ATP-binding site, thereby enhancing potency; however, their use is limited by higher toxicity and the emergence of new resistance mutations, such as C797S^[11,12]. Notably, the T790M mutation remains the most common mechanism of resistance to both first- and second-generation tyrosine kinase inhibitors (TKIs), occurring in approximately 50% of cases of resistance.^[13]

Osimertinib, a third-generation EGFR-TKI, was developed to target T790 M-mediated resistance while minimizing off-target effects^[14]. The phase III FLAURA trial confirmed its superiority over gefitinib or erlotinib as a first-line treatment for patients with classical EGFR mutations, demonstrating a significant improvement in progression-free survival (PFS)^[15]. Despite its clinical success, resistance continues to emerge—most often due to the C797S mutation, which interferes with Osimertinib's covalent binding. This mutation is responsible for up to 40% of cases of resistance to third-generation inhibitors^[16]. Consequently, novel fourth-generation EGFR inhibitors and alternative therapeutic strategies are being investigated^[17]. The ongoing emergence of drug-resistant EGFR mutations underscores the need for novel chemical scaffolds that can effectively and selectively inhibit EGFR across diverse mutation profiles.

Nitrogen-containing heterocyclic compounds have gained prominence in drug discovery due to their structural diversity, pharmacological versatility, and biological activity^[18,19]. Many heterocyclic rings, particularly those containing nitrogen, have been widely incorporated into anticancer drugs and are commonly found in FDA-approved therapies

[20]. Five-membered aromatic rings, such as 1,3,4-oxadiazoles and 1,3,4-thiadiazoles, have emerged as valuable pharmacophores in drug design due to their stability, metabolic resilience, and ability to form key hydrogen bonds and hydrophobic interactions with protein targets. Numerous studies have demonstrated the diverse biological activities of these heterocyclic compounds. [21,22]

1,3,4-Oxadiazole derivatives have emerged as promising anticancer agents due to their varied mechanisms of action and strong cytostatic potential. These five-membered heterocycles exhibit favorable pharmacokinetic properties, such as metabolic stability, and act as bioisostere for carbonyl-containing groups. Their anticancer effects are linked to the inhibition of multiple molecular targets, including EGFR, VEGFR, HDAC, PARP-1, and thymidylate synthase. Studies have shown that many oxadiazole-based compounds exhibit superior anti-proliferative activity compared to standard drugs, such as 5-

fluorouracil and cisplatin, across various cancer cell lines, including those of the breast, lung, liver, and colon. Owing to their multi-targeting nature and low toxicity, 1,3,4-oxadiazoles hold strong potential as scaffolds for the development of novel anticancer therapeutics. [23]

Akhtar et al. (2017) synthesized a series of benzimidazole-1,3,4-oxadiazole derivatives and assessed their cytotoxic activity against five human cancer cell lines: MCF-7 and MDA-MB231 (breast cancer), HaCaT (skin), HepG2 (liver), and A549 (lung). Among the tested compounds, compound 1 (bearing a para-chlorophenyl group) exhibited potent inhibition of EGFR and HER2 tyrosine kinases, with IC₅₀ values of 0.081 μM and 0.61 μM, respectively compound 2, featuring a para-methoxyphenyl substituent, exhibited the most potent cytotoxicity against the MCF-7 cell line, with an IC₅₀ of 2.55 μM, significantly outperforming the reference drug 5-fluorouracil. [24]

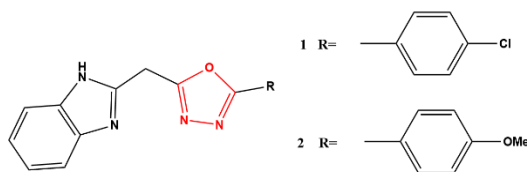


Figure 1. ???

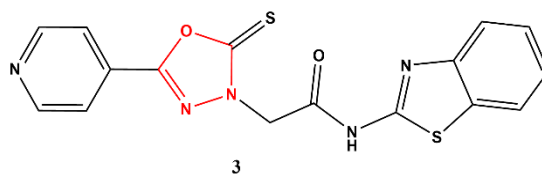


Figure 2. ????

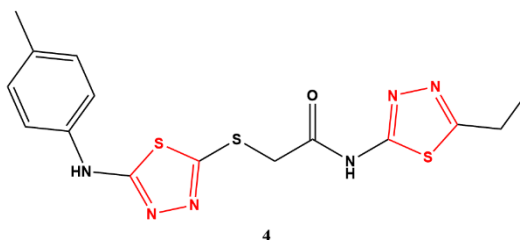


Figure 3. ??????

Bhanushali et al. (2017) synthesized a series of oxadiazole-thioacetamide derivatives targeting VEGFR kinase inhibition. Among them, compound 3 exhibited the most potent activity, demonstrating significant antiangiogenic effects in the Chick Chorioallantoic Membrane (CAM) assay compared to sorafenib. Moreover, the compound 3 showed

potent inhibition of VEGFR-2, with an IC₅₀ of 0.5 μM, highlighting its potential as an effective antiangiogenic agent in both the CAM and zebrafish embryo assays. [25]

1,3,4-thiadiazole derivatives exhibit notable biological activities, primarily attributed to the strong aromatic nature of their ring system. This

structural feature contributes to excellent in vivo stability and generally low toxicity in higher vertebrates, including humans, particularly when biologically active functional groups are attached to the aromatic ring. [26]

Studies by Çevik et al. (2020) demonstrated the potent antiproliferative activity of a new 1,3,4-thiadiazol derivative (compound 4), which exhibited significant cytotoxic activity, with an IC₅₀ of 0.084 ± 0.020 mmol/L against MCF-7 breast cancer cells and 0.034 ± 0.008 mmol/L against

A549 lung cancer cells, displaying superior potency in comparison to cisplatin. [27]

Atta-Allah et al. (2021) designed and synthesized various novel molecules based on 1,3,4-thiadiazole. The pharmacological activity of the synthesized compounds was assessed in vitro against four cancer cell lines (HepG2, MCF-7, HCT116, and PC-3) using the MTT method. Most compounds exhibited moderate to substantial anti-proliferative effects against the cancer cell lines, with compound (5) being the most effective. [28]

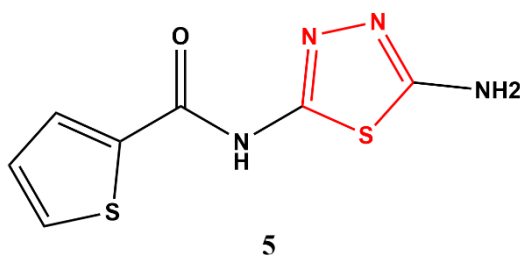


Figure 4. ??????

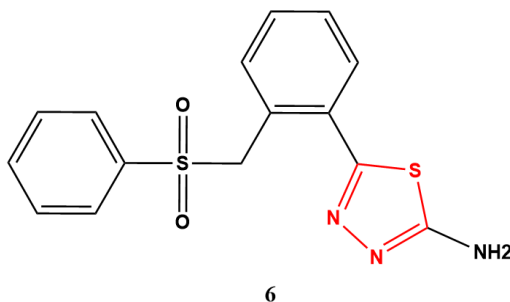


Figure 5. ?????

While Stecoza et al. (2023) demonstrate the importance of the 5-phenyl-1,3,4-thiadiazol-2-amine scaffold, they also highlight the promising antitumor capabilities of various novel compounds. Notably, compound (6) exhibits significant activity as an anti-proliferative agent, showing IC₅₀ values of 2.44 μM and 23.29 μM for LoVo and MCF-7 cells, respectively, after a 48-hour treatment period. [29]

These reports support the anticancer potential of 1,3,4-oxadiazole and 1,3,4-thiadiazole scaffolds.

Drug discovery is a multifaceted and time-intensive process that progresses through distinct stages, including target identification, lead optimization, preclinical testing, and clinical trials. To streamline early-stage screening and reduce experimental burdens, computational approaches such as molecular docking, molecular dynamics (MD) simulations, and ADMET (absorption, distribution,

metabolism, excretion, and toxicity) predictions have become essential components of modern drug design. [30]

Molecular docking is a cornerstone of structural biology and computer-aided drug design. It is a computational algorithm used to assist in determining the preferred conformation or binding site of a small molecule with its macromolecular target, as well as in analyzing protein-ligand interactions by estimating their affinity. Therefore, this method is beneficial in identifying the biological activity of any lead compound and elucidating the structure-activity relationship. Additionally, it can contribute to increasing ligand affinity by manipulating select residues available at the binding site [31]. Molecular docking predicts the most favorable orientation and binding affinity of a ligand within the active site of a target protein,

enabling the identification of structurally and energetically optimal complexes. [32]

This is further validated through molecular dynamics (MD) simulations, which assess the stability, flexibility, and conformational behavior of receptor-ligand complexes over time under physiological conditions, utilizing Newtonian physics. [33]

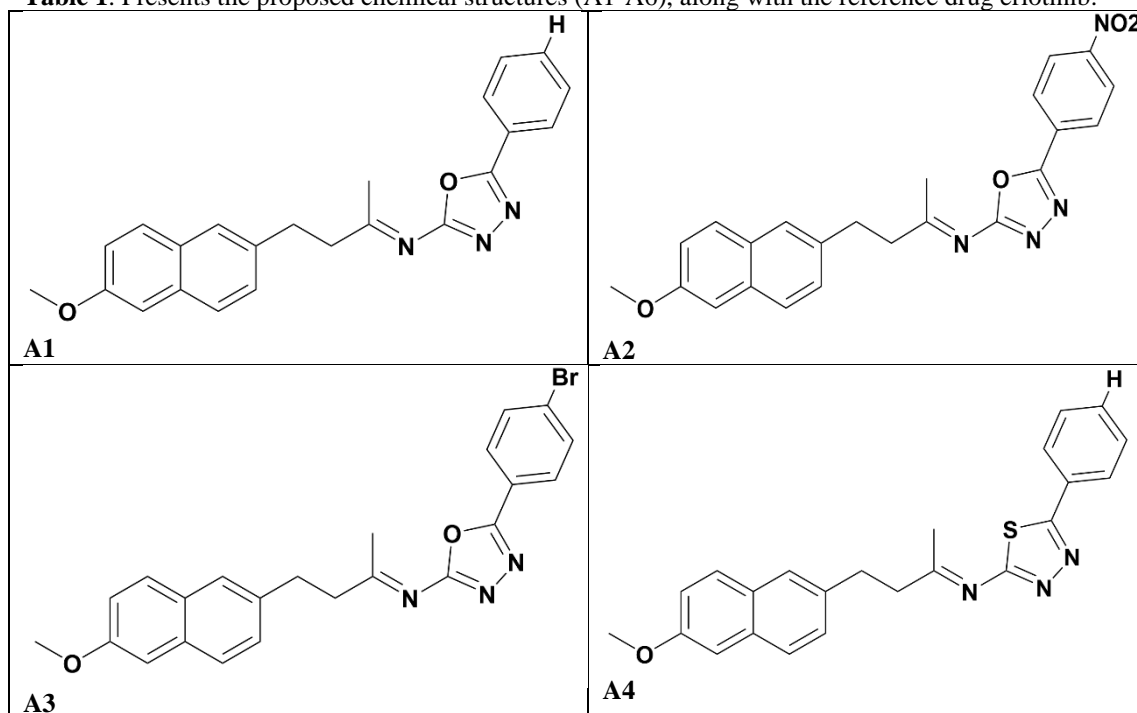
In parallel, *in silico* ADMET profiling enables the early prediction of pharmacokinetic properties, including gastrointestinal absorption, blood-brain barrier permeability, metabolic stability, and toxicity. These parameters are crucial for selecting compounds with favorable drug-likeness, bioavailability, and safety profiles. [34]

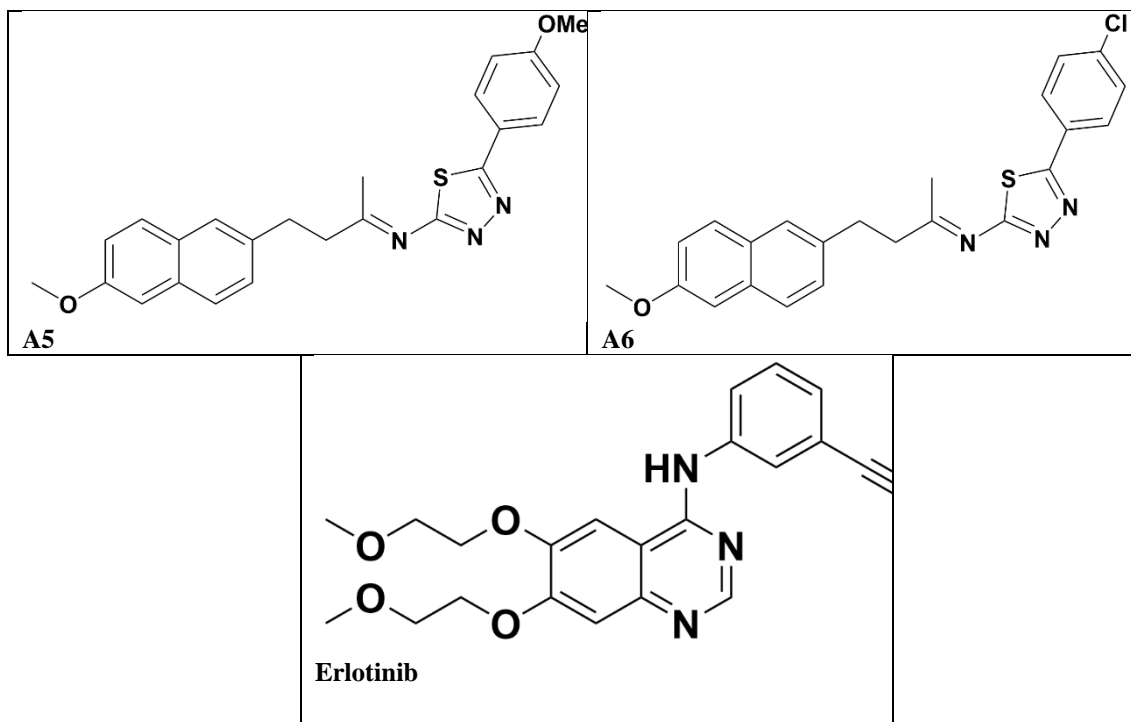
Together, these *in silico* methods accelerate the identification of promising drug candidates by minimizing costly laboratory experimentation and highlighting molecules with optimal pharmacodynamic and pharmacokinetic attributes. In this study, a novel series of 1,3,4-oxadiazole and 1,3,4-thiadiazole derivatives (A1-A6) was

theoretically designed by the authors through rational drug design, informed by an extensive literature review. These structures were developed to target the epidermal growth factor receptor (EGFR). The objective for this work is to evaluate binding affinity, pharmacokinetic behavior, and dynamic stability of designed compounds using an integrated *in silico* approach. Molecular docking, ADMET profiling, and molecular dynamics (MD) simulations were employed to predict EGFR-binding capacity, drug-likeness, and conformational stability. This strategy aims to identify promising, receptor-specific molecules with favorable pharmacokinetic profiles, providing a rational foundation for future synthesis and experimental validation.

To provide an apparent visual reference for the molecular design of the tested compounds, the 2D structures of the newly designed ligands (A1-A6) along with the reference inhibitor Erlotinib are presented in Table 1.

Table 1. Presents the proposed chemical structures (A1-A6), along with the reference drug erlotinib.





2. Computational Method

All molecular modeling, docking, and simulation studies were performed using professional-grade computational chemistry software, including ChemOffice Suite, Schrödinger Suites, and GOLD.

2.1. ADMET Profile

To evaluate these novel compounds, this study employs a comprehensive set of computational techniques that mimic the complex interactions within biological systems and predict the efficacy and safety profiles of potential drug candidates. The Absorption, Distribution, Metabolism, and Excretion (ADME) studies are crucial first steps, utilizing tools like Schrödinger Suites to predict the pharmacokinetic properties of the compounds, ensuring they possess desirable attributes such as good bioavailability and appropriate metabolism. This process involves identifying one of the most effective pharmaceutical candidates by selecting safe compounds and eliminating others with poor ADMET properties, which are more likely to fail in the later stages of the drug development process^[35]. After preparing the proposed compounds using ChemDraw and the LigPrep tool, we ran the QikProp tool to generate the result as an Excel file. ADMET profiling was conducted using QikProp within Schrödinger Suites. Each proposed compound was evaluated for key pharmacokinetic properties such as:

- Lipinski's Rule of Five includes molecular weight, hydrogen bond acceptors and donors, LogP, and rotatable bonds.
- Human Oral Absorption and predicted CNS permeability (LogBB).
- Caco-2 and MDCK cell permeability, Serum Albumin Binding, Metabolic Reactions, and hERG inhibition risk (QPlogHERG).

2.2. Molecular Docking

A standard process of molecular docking consists of three main steps: preparing the receptor and ligand molecules, executing the actual docking using a specific algorithm, and conducting post-docking analysis to determine the optimal binding pose and evaluate the binding affinity of the target ligand and receptor.^[31]

Molecular docking was conducted using the GOLD Suite 2022.3.0 (Cambridge Crystallographic Data Centre) to evaluate the binding affinity and orientation of the newly designed 1,3,4-oxadiazole and 1,3,4-thiadiazole derivatives (A1-A6) against the epidermal growth factor receptor (EGFR). The crystal structure of EGFR in complex with erlotinib (PDB ID: 4HJO) was retrieved from the Protein Data Bank and used as the receptor model.

By using Hermes software, all missing hydrogen atoms were added, and all non-essential water molecules, except for HOH 1104, were removed.

The crystallographic water molecule HOH 1104 was intentionally retained due to its critical role in stabilizing ligand–protein interactions within the active site of the EGFR tyrosine kinase domain (PDB ID: 4HJO). Specifically, the co-crystallized inhibitor erlotinib forms a key water-mediated hydrogen bond bridge via HOH 1104 with residues THR830 and THR766, which are essential for anchoring the ligand within the binding pocket.

Removal of this water molecule would disrupt this conserved interaction network, potentially compromising the biological relevance of the docking results. This decision aligns with structural insights from the RCSB Protein Data Bank [36,37]. And previous literature [38,39] emphasizes the importance of HOH-1104 in mediating EGFR-ligand recognition. [39]

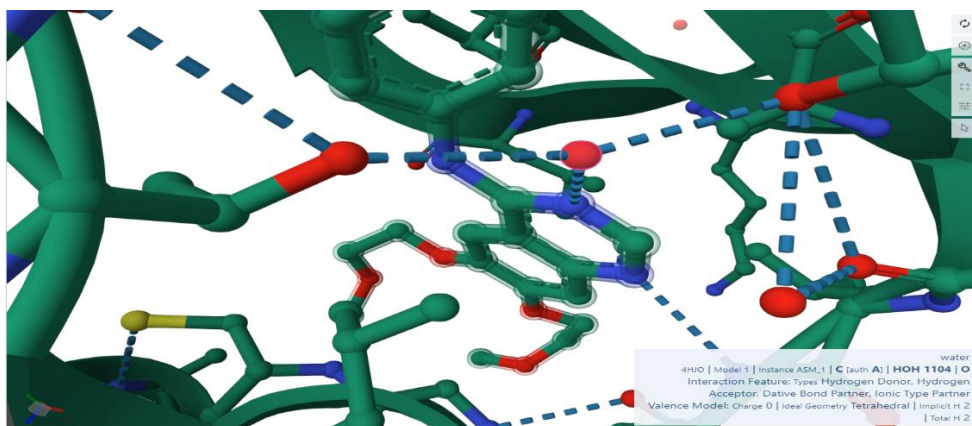


Figure 1. Binding interactions of erlotinib within the EGFR active site (PDB ID: 4HJO), highlighting the role of HOH 1104 in bridging hydrogen bonds to THR830 and THR766. Image from the RCSB Protein Data Bank (RCSB.org) of PDB ID: 4HJO. [36]

The size used for the grid box in docking is a 10 Å radius of the co-crystallized reference ligand in the EGFR tyrosine kinase domain (PDB ID: 4HJO). The GOLD docking algorithm employs a Genetic Algorithm (GA) for conformational sampling and pose optimization, where each docking solution (chromosome) encodes the ligand’s hydrogen bonding, hydrophobic mapping, and torsional flexibility. The algorithm iteratively improves the population based on fitness scores through crossover, mutation, and migration operations. ChemPLP serves as the scoring function, evaluating interactions based on piecewise linear potentials that account for protein-ligand interactions involving van der Waals forces, hydrogen bonding, and steric complementarity. The automatic (ligand-dependent) GA setting is applied to ensure efficient pose sampling, taking into account ligand flexibility and the number of rotatable bonds. The search efficiency is set to 100%, resulting in an estimated 30,000 operations per ligand. Atomic partial charges are automatically assigned during ligand and protein preparation using the software’s default parameterization protocols.

The chemscore_kinase template was applied, with early termination disabled, and the speed docking setting was set to “slow” to prioritize accuracy.

The top-ranked pose of each ligand, based on the ChemPLP fitness score (used as a scoring function in GOLD docking, is a dimensionless scoring function. It does not have a unit such as kcal/mol or kJ/mol. It is a relative numerical value derived from a piecewise linear potential that combines terms modeling van der Waals interactions, hydrogen bonding, and protein-ligand complementarity. Where higher values indicate more favorable protein-ligand interactions as predicted by the GOLD scoring algorithm, was selected for further analysis of binding interactions and comparison with the reference inhibitor erlotinib. [40]

where;

W_{PLP} : Weight applied to the PLP score

f_{PLP} : Piecewise Linear Potential - models steric complementarity between the ligand and protein

$W_{lig-clash}$: Weight for ligand clash penalty

$f_{lig-clash}$: Ligand clash term - penalizes heavy-atom clashes within the ligand

$W_{lig-tors}$: Weight for torsional strain

$f_{\text{lig-tors}}$: Ligand torsional strain -penalty for unfavorable torsional angles in the ligand

$f_{\text{chem-cov}}$: Covalent interaction penalty - used in covalent docking

W_{Prot} : Weight for flexible side chain interactions

$f_{\text{chem-prot}}$: Flexible protein side-chain term - allows protein flexibility in binding site residues

W_{cons} : Weight applied to constraint penalty

f_{cons} : Constraint penalty - penalizes violation of user-defined constraints

$$\text{fitness}_{\text{SPLP}} = - (W_{\text{PLP}} \cdot f_{\text{PLP}} + W_{\text{lig-clash}} \cdot f_{\text{lig-clash}} + W_{\text{lig-tors}} \cdot f_{\text{lig-tors}} + f_{\text{chem-cov}} + W_{\text{Prot}} \cdot f_{\text{chem-prot}} + W_{\text{cons}} \cdot f_{\text{cons}})$$

2.3. Molecular Dynamics Simulation

Molecular dynamics simulations utilized the Desmond engine within the Schrödinger Suite.

The crystal structure of the EGFR tyrosine kinase domain (PDB ID: 4HJO), co-crystallized with erlotinib, was retrieved from the Protein Data Bank and prepared using the Protein Preparation Wizard in Maestro (Schrödinger Suite 2022-3). The preprocessing involved assigning bond orders, adding missing side chains, optimizing hydrogen bonding networks, and removing all hydrogens, followed by reassignment. Crystallographic water molecules located more than 5 Å from the co-crystallized ligand were removed. The structure was energy minimized using the OPLS4 force field, with a convergence root-mean-square deviation (RMSD) cutoff of 0.30 Å.

The system was constructed using the System Builder, placing the protein–ligand complex in a cubic simulation box with a 10 Å buffer on all sides and solvating it with the SPC water model. Periodic boundary conditions (PBC) were applied. The addition of five Cl^- ions neutralized the net charge of the system, which was initially +5. An additional 27 Na^+ and 27 Cl^- ions were introduced to simulate 0.15 M NaCl, representing physiological conditions.

The system underwent a standard relaxation protocol, including restrained energy minimization, followed by two equilibration stages: 1 nanosecond under the NVT ensemble (constant number of particles, volume, and temperature) to stabilize the temperature, and one nanosecond under the NPT ensemble (constant number of particles, pressure, and temperature) to equilibrate the system's pressure. The NPT ensemble was also used during the production run to maintain constant temperature and pressure, allowing the simulation box volume to adjust in response to internal fluctuations. This ensemble is widely regarded as appropriate for mimicking physiological conditions, ensuring

accurate representation of system density and pressure throughout the simulation. [41]

The production simulation was conducted for 100 nanoseconds using the NPT ensemble at a constant temperature of 300 K, regulated by the Nose-Hoover thermostat, and a pressure of 1.01325 bar, controlled by the Martyna-Tobias-Klein barostat.

Long-range electrostatic interactions were calculated using the Particle Mesh Ewald (PME) method, applying a 10 Å cutoff for short-range van der Waals and Coulomb interactions. Trajectory frames were recorded at intervals of 4.8 picoseconds.

Post-simulation analyses were conducted using Maestro's Simulation Interaction Diagram tool. Parameters evaluated included protein and ligand RMSD, residue RMSF, ligand RMSF, protein–ligand contacts (hydrophobic, ionic, water bridges), and torsional flexibility.

3. Results and discussion

3.1. ADMET Profile results

These initial results from the Maestro study provide valuable insights into the pharmacokinetic properties of the compounds. As shown in Table 2, Lipinski's Rule of Five [42], Table 3, Structural Properties, and Table 4, Pharmacokinetics properties.

The molecular weight (M.W.) of the newly proposed compounds and the reference compound (Erlotinib) falls within the suitable range for drug-likeness (≤ 500 g/mol), which contributes to good oral bioavailability. Most of the compounds also comply with Lipinski's Rule of Five regarding the number of hydrogen bond acceptors (HBAs) and donors (HBDs), indicating suitable permeability and absorption. Consequently, values remained within the ≤ 10 and ≤ 5 thresholds, respectively. The LogP of all compounds (including Erlotinib) is below the accepted threshold (≤ 5), indicating appropriate lipophilicity that supports membrane permeability without compromising solubility. The

Ahmed Haloob Kadhim, Monther Faisal Mahdi, Ayad MR Raauf

number of rotatable bonds, a measure of molecular flexibility, also stays below 10, suggesting that the compounds may exhibit a good level of conformational adaptability for binding while maintaining drug-like properties. Although the

proposed compounds comply with the Rule of Five, Erlotinib slightly breaches it. Nevertheless, this breach does not necessarily impede its therapeutic effectiveness.

Table 2. Lipinski's rule of five for proposed compounds and reference inhibitor Erlotinib.

Parameter	Accepted Range	A1	A2	A3	A4	A5	A6	Reference
M.W	≤500 g/mol	371.4	416.43	450.33	387.4	417.5	421.9	393.4
HBAs	≤10	4.25	5.25	4.25	3.75	4.5	3.75	7.4
HBDs	≤5	0	0	0	0	0	0	1.5
LogP	≤5	4.19	3.76	4.57	4.14	4.34	4.41	3.67
Rotatable Bonds	≤10	6	6	7	6	6	7	11
Rule of Five	Compliant	Yes	Yes	Yes	Yes	Yes	Yes	No

M.W: Molecular Weight (g/mol); HBAs: Hydrogen Bond Acceptors; HBDs: Hydrogen Bond Donors; LogP: Partition Coefficient; Rotatable Bonds: Number of rotatable bonds.

Table (3): Structural Properties for proposed compounds and reference inhibitor Erlotinib.

Parameter	Accepted Range	A1	A2	A3	A4	A5	A6	Reference
Human Oral Absorption	-	High	High	Low	High	Low	Low	High
LogBB	-3.0 to 1.2	-0.364	-1.141	-0.35	-0.273	-0.243	-0.109	-0.506
Molecular Volume	<1500 Å ³	1214.8	1208.1	1299.9	1237.0	1337.37	1280.8	1316.85
PSA	<140 Å ²	61.52	105.66	63.56	51.33	59.25	51.33	63.3
Dipole Moment	<10 Debye	4.811	8.153	4.768	4.552	2.683	5.124	5.631
Globularity	Closer to 1	0.845	0.874	0.766	0.824	0.788	0.814	0.766

LogBB: Brain/blood partition coefficient; PSA: Polar Surface Area (Å²); Dipole Moment: Molecular polarity (Debye); Globularity: Shape compactness.

Table (4): Pharmacokinetic properties for proposed compounds and reference inhibitor Erlotinib.

Parameter	Accepted Range	A1	A2	A3	A4	A5	A6	Reference
Caco-2 Permeability	>500	2636.5	400.3	2383.4	3172.0	3833.2	3175.5	4528.36
MDCK Permeability	>500	1410.7	183.9	3352.2	2088.9	3231.6	5151.3	2531.30
Serum Albumin Binding	-	0.753	0.424	1	0.951	0.999	1.079	0.236
Metabolism Reactions	Fewer reactions better Concern	4	5	4	4	5	4	6
QPlogHERG	below -5	-5.792	-4.89	-7.198	-6.197	-6.586	-6.122	-6.903

Caco-2 Permeability: permeability through Caco-2 cells (nanometers per second); MDCK Permeability: permeability in MDCK cells (nanometers per second), indicating general cellular permeability; Metabolic Reactions: Predicted biotransformation; QPlogHERG: Predicted cardiotoxicity.

An assessment of the proposed compounds and the reference, Erlotinib, indicates adherence to significant pharmacokinetic parameters. All the compounds exhibit oral absorption in humans, although the extent of this absorption varies.

Brain/Blood Barrier Penetration (LogBB)-as LogBB, which is a desirable attribute as it allows for targeting of peripheral tissue without the side effects characteristic of the CNS, the LogBB values for the designed compounds A1-A6 ranged from -

1.141 to -0.243, indicating generally limited to moderate ability to cross the blood-brain barrier (BBB) [43,44]. Precisely, compound A2 (-1.141) is predicted to have poor CNS penetration, while compounds A4 (-0.273), A5 (-0.243), and A6 (-0.109) exhibit better BBB permeability, suggesting potential for partial CNS access. The reference compound, Erlotinib, exhibited a LogBB of -0.506, positioning it within the moderate range of CNS penetration. This requirement is met by the Molecular Volume for all compounds, including Erlotinib, due to the limitations of solubility and Permeability [45]. Regarding PSA (which should be <140 Å² for good permeability of compounds into cellular membrane), all compounds fit nicely within an acceptable range below 140 Å² [46]. The Dipole Moment, preferably <10 Debye, indicates polarity; most compounds exhibit low values, but A2's greater polarity (8.153) may hinder its ability to cross membranes compared to Erlotinib. Lastly, in terms of Globularity, values close to 1 indicate a compact and stable molecular structure, which is a positive attribute for each of the compounds, including Erlotinib, suggesting that, at least in a physical and chemical sense, all compounds can interact with a biological target. Overall, the compounds appear promising in terms of their pharmacokinetic profile and are generally comparable to Erlotinib.

Reactions: Predicted biotransformation;
QPlogHERG: Predicted cardiotoxicity.

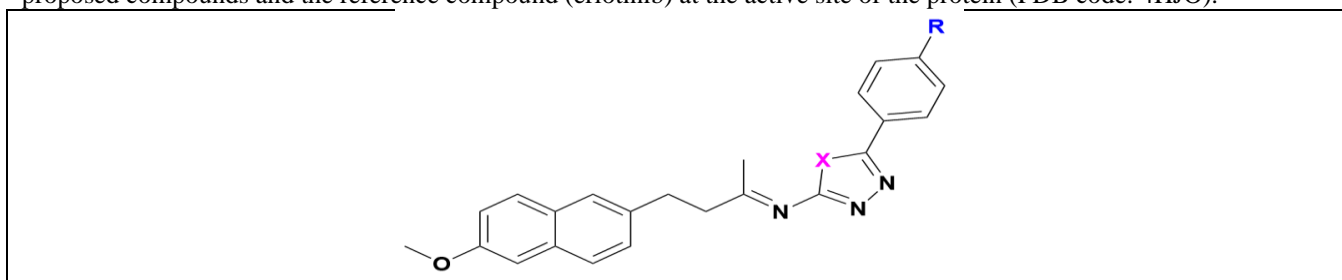
Most of the proposed compounds, including A1, A3, A4, and A5, exhibit high Caco-2 permeability (>500 nm/s) [44, 47], suggesting favorable intestinal absorption profiles. In contrast, compound A2 demonstrated a markedly lower permeability (400.3 nm/sec), indicating limited intestinal absorption and potentially reduced oral bioavailability. Similarly,

MDCK permeability values for A3 (3352.2 nm/sec) and A5 (3231.7 nm/sec) reflect excellent cellular permeability, whereas A2 again recorded the lowest permeability (183.9 nm/sec), reinforcing its comparatively poor membrane transport characteristics among the tested candidates. A3 and A5 bound serum albumin the most (1 and 0.999, respectively), which may improve distribution but delay release at the target site [48, 49]. All of the compounds exhibit acceptable metabolic reactions (4-5), indicating moderate metabolic stability. For QPlogHERG [44, 50], A1, A2, and A4 show a low cardiotoxicity risk. A1, A3, and A4 exhibited a similar pharmacokinetic profile to Erlotinib, characterized by good absorption, effective penetration, and metabolic stability. However, A2 is an exception, with relatively low permeability and poor binding to albumin, rendering it the least promising candidate for clinical advancement. Overall, A1, A3, and A4 stand out as good candidates that are compatible with Erlotinib's favorable pharmacokinetic properties.

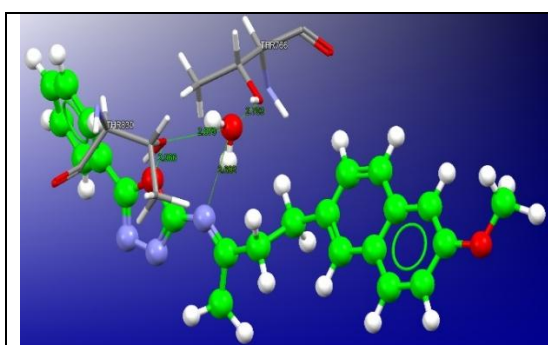
3.2. Molecular Docking

Molecular docking data revealed the strength and stability of receptor–ligand binding interactions. The average score for binding affinity, measured as PLP fitness, ranged from 80.38 to 90.61 for all compounds on EGFR, while erlotinib's average score was 77.62. The scores (PLP fitness) were notably high (90.61 and 83.77, respectively) for the newly introduced compounds (A1 and A2), reflecting their exceptional binding affinity and satisfactory orientation in the receptor's binding site among the studied compounds, as shown in Table 5 and Figure 2.

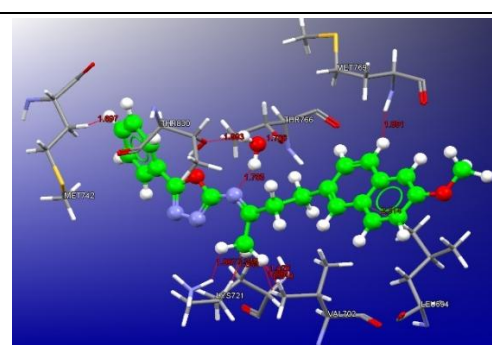
Table (5): This table presents the proposed compound structure and its derivatives, as well as the interaction between the proposed compounds and the reference compound (erlotinib) at the active site of the protein (PDB code: 4HJO).



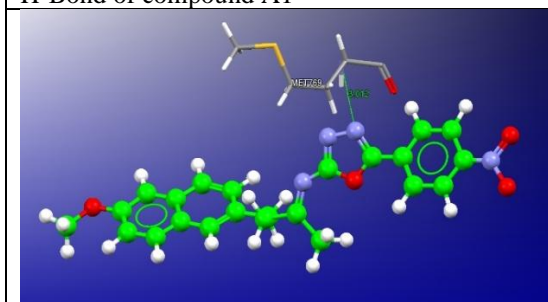
Compound	Interaction of the proposed compounds and the Reference Compound with the amino acid within the active site of the protein (PDB code: 4HJO)		
	H-Bond	Short Contact	PLPfitness Score (average Value)
A1 (X=O / R= H)	oxadiazole...THR830 imine...HOH1104...THR830, THR766	MET742, MET769, LEU694, VAL702 (3), LYS721 (3), imine...HOH1104...THR830, THR766	90.61
A2 (X=O / R= NO ₂)	oxadiazole...MET769	MET742 (2), LEU834, LEU764 (3), MET769, VAL702 (4), HOH1104...THR766, THR830	83.77
A3 (X=O / R= Br)	oxadiazole...THR830, HOH1104...THR766, THR830	MET742, VAL702 (3), THR830, LEU820, LEU694 (2), HOH1104...THR766, THR830	80.38
A4 (X=S / R= H)	thiadiazole...THR830	LEU820, THR830 (2), MET742, LEU764, LEU694, VAL702 (5)	80.51
A5 (X=S / R= OCH ₃)	thiadiazole...THR830, HOH1104...THR830, THR766	VAL702, LEU820, LYS721 (2), THR830 (3), HOH1104...THR830, THR766	80.41
A6 (X=S / R= Cl)	thiadiazole...THR830	ASP831 (3), LEU764, THR830, LEU820, VAL702 (2), LEU694	80.91
Reference compound (Erlotinib)	quinazoline...HOH1104...THR830, THR766	GLY695 (3), VAL702 (2), ASP776, CYS773 quinazoline...HOH1104...THR830, THR766	77.62



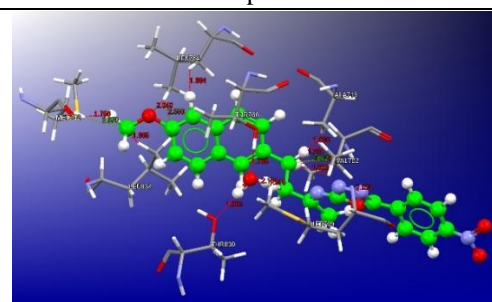
H-Bond of compound A1



Short Contact of Compound A1



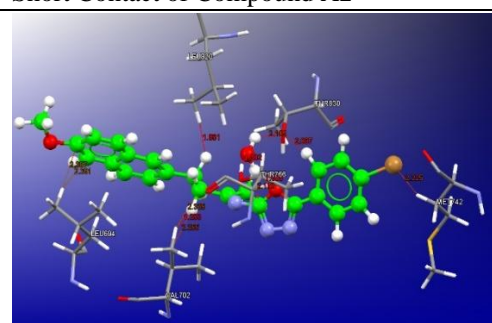
H-Bond of compound A2



Short Contact of Compound A2



H-Bond of compound A3



Short Contact of Compound A3

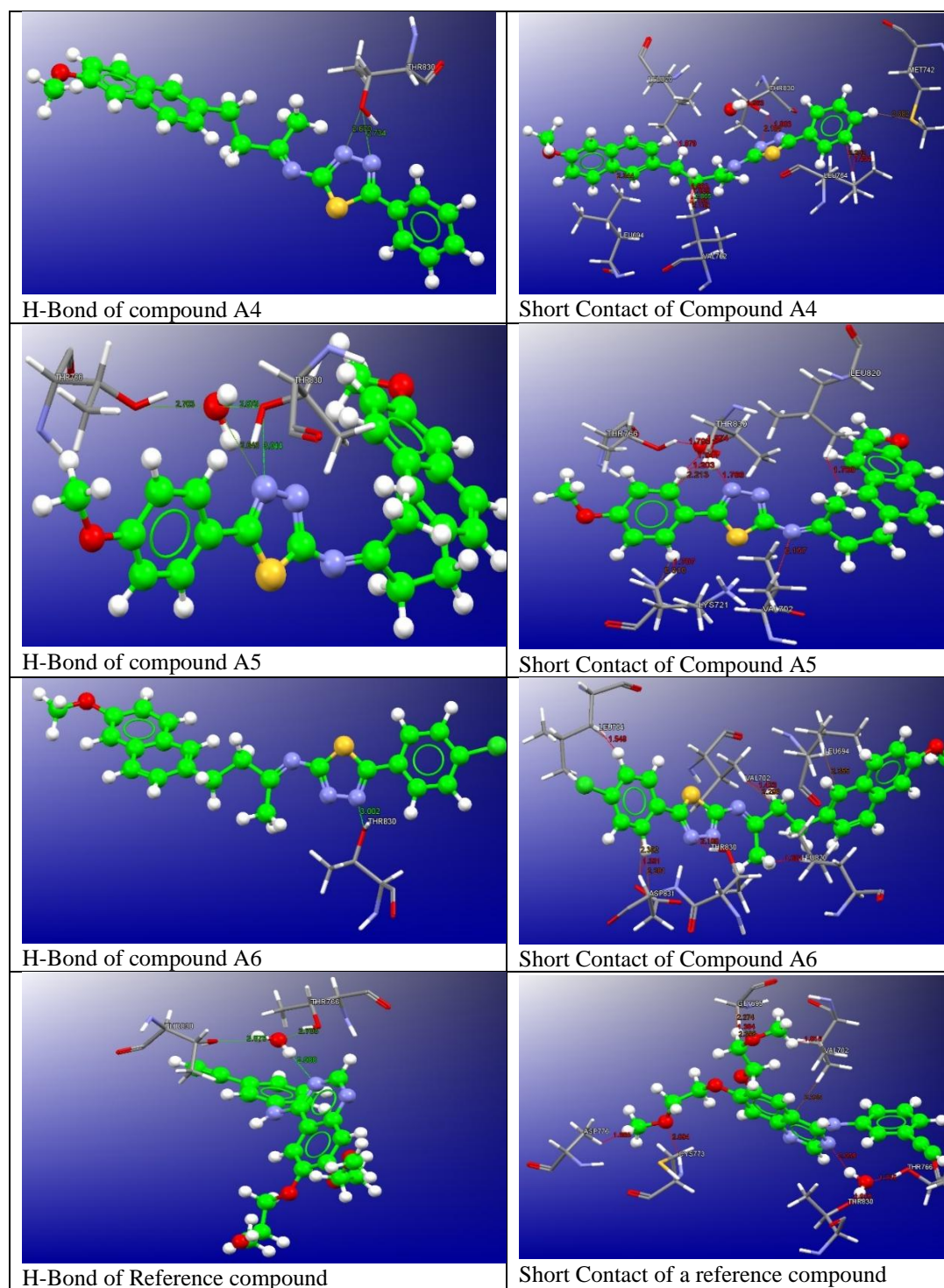


Figure (2): 3D visualization of proposed compounds and erlotinib bound to EGFR (PDB ID: 4HJO), generated using GOLD. Ligands are shown as stick-and-ball models, while the receptor is depicted as capped sticks. Green dashed lines indicate hydrogen bonds; red dashed lines denote short contacts.

The molecular docking study demonstrated that the binding affinity scores of the proposed 1,3,4-oxadiazole and 1,3,4-thiadiazole derivatives (A1-A6) ranged from 80.38 to 90.61, with A1 (90.61) and A2 (83.77) outperforming the reference

compound, Erlotinib (77.62). These superior scores were attributed to the strong hydrogen bonds and hydrophobic interactions between the ligands and the active site residues of EGFR. For instance, A1 exhibited significant hydrogen bond interactions

with THR830 and THR766 through the oxadiazole oxygen and imine nitrogen, alongside extended hydrophobic interactions with MET742, MET769, and LYS721. Similarly, A2 was found to engage in hydrogen bonding via its oxadiazole nitrogen, as well as hydrophobic interactions with MET742 and VAL702. The thiadiazole derivatives (A3-A6) displayed good binding affinities, although lower than those of A1 and A2, indicating the influence of functional groups on binding stability. The developers of the proposed compounds experienced stronger interactions and better binding orientations compared to Erlotinib, which formed only a single hydrogen bond and exhibited moderate hydrophobic interactions. These findings suggest that the oxadiazole and thiazole scaffolds may enhance the affinity of the ligands, providing a valuable foundation for the rational design of new EGFR inhibitors. The docking phase was crucial, offering a static view and correlated structures; however, dynamic interactions and experimental validation are also necessary to affirm the docking results.

3.3. Molecular Dynamics Simulations

Using molecular dynamics (MD) simulations, we examined the dynamic nature and stability of the A1-EGFR protein-ligand complex over time. The choice of Compound A1 for molecular dynamics simulation is based on its optimal molecular docking and ADMET profile analyses, which predict its potential as a highly effective EGFR inhibitor. A1 achieved the highest PLP fitness score (90.61), which is 12.99 points higher than that of the reference compound, Erlotinib (77.62). This improved score is attributed to the strong interaction between A1 and the EGFR active site, specifically hydrogen bonding between the oxygen of the oxadiazole and the nitrogen of the imine, involving the THR830 and THR766 residues, respectively. A1 also generated significant hydrophobic interactions with the key residues MET742, MET769, and LYS721, enhancing binding stability and selectivity.



Simulation Interactions Diagram Report

Simulation Details

Jobname: haloob-desmond_md_job_1
Entry title: 4hjo - minimized Structure1

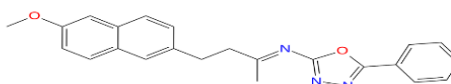
CPU #	Job Type	Ensemble	Temp. [K]	Sim. Time [ns]	# Atoms	# Waters	Charge
1	mdsim	NPT	300.0	100.102	34019	9792	0

Protein Information

Tot. Residues	Prot. Chain(s)	Res. in Chain(s)	# Atoms	# Heavy Atoms	Charge
278	'A'	ict_values([278])	4535	2232	+5
679	A	680 685 690 695 700 705 710 715 720 725 730 735 740 745	LLRLKRETEFKRIKVLGSGAFGTVYKGLWIPVKIPVAIKELREATSPKANKEILDEAYVMASVDNPHVCR	752	SSA
753	A	755 760 765 770 775 780 785 790 795 800 805 810 815	LLGICLTSVQLIIFOLMPEGCLLDYVVRHKDNLGSGOYLLNWCVOIFAGWNYLEDRLVHRDLAARNVLVK	822	SSA
823	A	825 830 835 840 845 850 855 860 865 870 875 880 885	TPQHVKITDFGLAKLLGAEKEYHAEKGVPIKWMALLESILHRIYTHQSDVWSYGVTVWELMTFGSKPYD	892	SSA
893	A	895 900 905 910 915 920 925 930 935 940 945 950 955	GI FASEI SSI LEKGERLPPOPICTIDVYNI MRK CWMI DADSPKPRELIEFSPMARDPQRYVIQGG	960	SSA

Ligand Information

SMILES	COC(c1)cc(c12)ccc(c2)CC/C(C)=N/c(o3)nnc3-c4cccc4
PDB Name	'UNK'
Num. of Atoms	49 (total) 28 (heavy)
Atomic Mass	371.443 au
Charge	0
Mol. Formula	C23H21N3O2
Num. of Fragments	2
Num. of Rot. Bonds	6



Counter Ion/Salt Information

Type	Num.	Concentration [mM]	Total Charge
Cl	32	59.418	-32
Na	27	50.134	+27

Figure 3. Molecular Dynamics Diagram Report includes Simulation details, protein information, and ligand information.

In the ADMET profile analysis, A1 demonstrated highly favorable pharmacokinetic properties, including high human oral absorption and an

appropriate molecular weight (371.44 g/mol), which support good oral bioavailability. It has a LogP value of 4.19 (a quantitative coefficient of the

lipophilicity of a substance), thereby complying with Lipinski's Rule of Five. A1 also exhibited moderate metabolic stability with four predicted metabolic reactions, and high Caco-2 cell permeability (2636.59 nm/sec), which suggests good intestinal absorption. These attributes make A1 a significant contender for further consideration.

3.3.1. Root Mean Square Deviation (RMSD)

The first output is the Root Mean Square Deviation (RMSD) over time, which measures the average displacement of selected atoms in angstroms over a 100-nanosecond period, as illustrated in Figure 4.

The RMSD fluctuates between 1 and 3 Å, which is within the commonly accepted range for structural stability in protein–ligand complexes. Previous molecular dynamics studies have reported average RMSD values stabilizing around 2.11 Å for EGFR–ligand systems, indicating consistent and stable binding throughout the simulation period [51]. Similarly, other studies have demonstrated stable complexes with RMSD fluctuations ranging from 0.5 to 2.5 nm (5–25 Å) [52], while some have indicated stability when the RMSD levels off at around 0.3 nm (3 Å) [53].

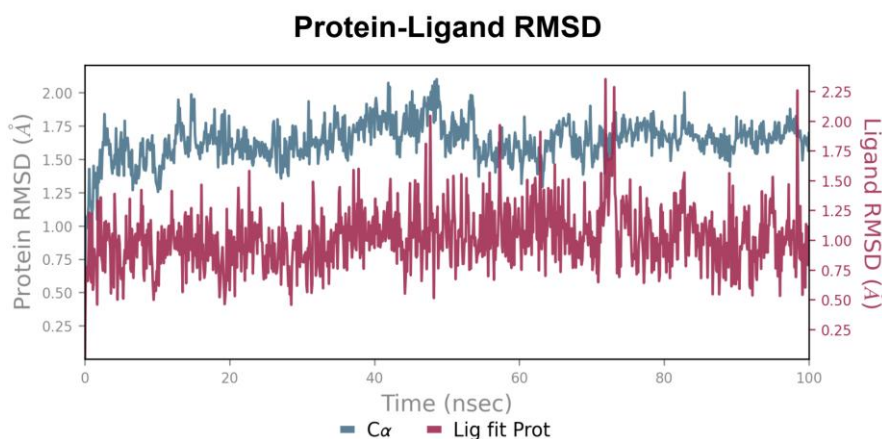


Figure (4): RMSD of the atoms of protein and the ligand over time (A1-EGFR).

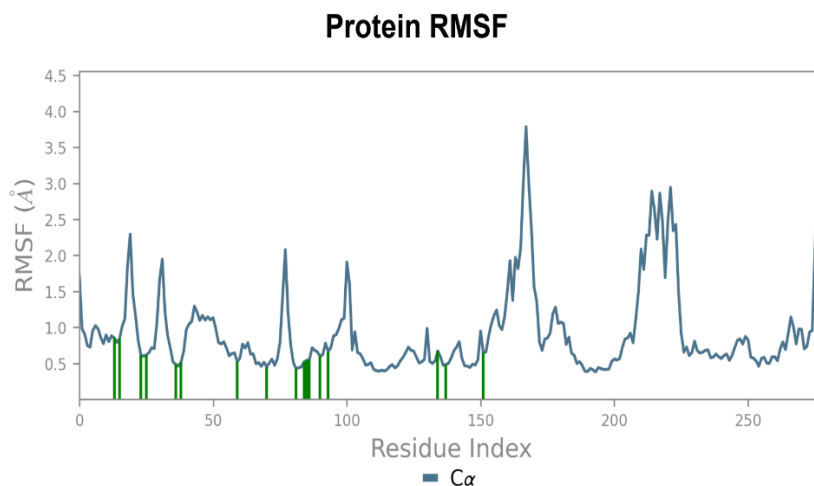


Figure (5): protein RMSF shows the stability of the protein, and the green line represents the contact with Compound A1 during the Simulation.

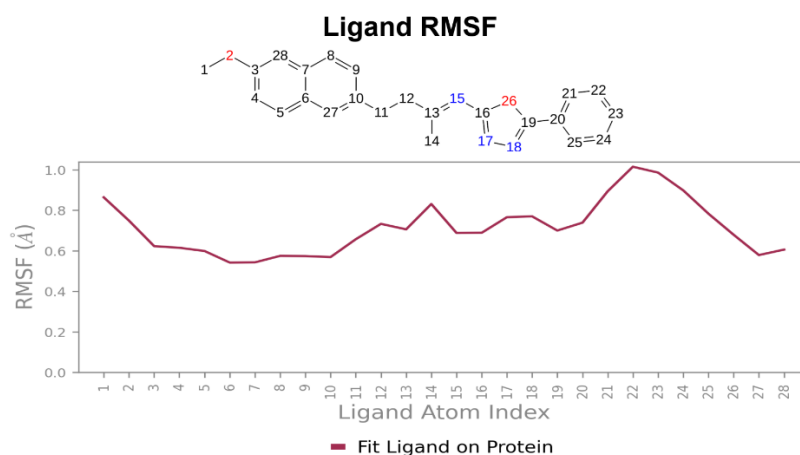


Figure (6): Ligand RMSF showing the Fluctuation of each atom of Compound A1 within the active site during simulation.

Protein RMSD stabilized between 1-3 Å during the 100-ns simulation, indicating that the protein maintained its structural integrity throughout the trajectory. The stabilization of Protein RMSD demonstrates that the system remained stable during the simulation. This supports the reliability of the simulation data, as shown in Figure 4.

Ligand RMSD: The Ligand RMSD remained consistent relative to the protein backbone throughout the 100-ns simulation, showing no significant deviations. This indicates that the ligand (A1) stayed stably bound within the binding pocket. The low Ligand RMSD emphasizes the strong affinity and stable binding of A1 to the EGFR binding pocket. This stability is essential for the effective inhibition of EGFR activity, confirming A1's potential as a therapeutic agent, as shown in Figure 4.

3.3.2 Root Mean Square Fluctuation (RMSF)

Protein RMSF: The Root Mean Square Fluctuation (RMSF) of the protein provides insight into localized changes along its chain during the simulation- the peaks on the graph highlight areas where the protein undergoes considerable fluctuations. In the Ligand Contacts analysis, the protein residues interacting with the ligand are depicted as green vertical bars. This analysis reveals that the amino acids of the protein that interact with the ligand maintain a distance of less than 1 Å, indicating that the binding groups of A1 have stable interactions with the protein's amino acids, as shown in Figure 5. The high value of RMSF shows

the flexible region. In contrast, the low RMSF value indicates limited movements during the MD simulation. A fluctuation value of less than 2 Å is acceptable for a small protein. ^[54]

Ligand RMSF: The Ligand Root Mean Square Fluctuation (L-RMSF) is an effective metric for assessing the positional changes of ligand atoms throughout the simulation. This metric provides crucial insights into the interactions between ligand fragments and the protein, as well as their entropic effects on binding. The analysis begins with the alignment of the protein-ligand complex using the protein backbone, followed by an evaluation of the ligand's root mean square fluctuation (RMSF) based on its heavy atoms. Figure 6 illustrates that the RMSF values for Compound A1 are below 1.0 Å, which signifies the ligand's stability within the protein active site.

3.3.3 Protein Secondary Structure

The secondary structure of EGFR remained essentially unchanged, with 46.56% of residues in stable secondary structure elements (32.18% helices and 14.39% strands). This retention of secondary structure indicates that EGFR maintains its structural integrity throughout the simulation. This is crucial for ensuring reliable binding evaluations, as significant structural changes can significantly influence interaction profiles with ligands, as shown in Figures 7A and 7B.

3.3.4 Protein-Ligand Contacts

The simulation revealed persistent interactions between A1 and key EGFR residues, including

Ahmed Haloob Kadhim, Monther Faisal Mahdi, Ayad MR Raauf

hydrogen bonds, hydrophobic contacts, and water bridges. Contact stability.

A stable contact was observed, particularly between LEU694 and MET769, which provided further stabilization to the protein-ligand complex, as shown in Figure 8.

Protein-ligand contact histogram: This illustrates the distribution of water bridge contacts with MET769, ASP817, and LEU694, as well as hydrophobic interactions with LEU694, LYS721, and LEU764, both of which significantly contribute to stabilizing the complex, as shown in Figure 9.



Figure (7A): Protein secondary structure elements (SSE) during simulation.

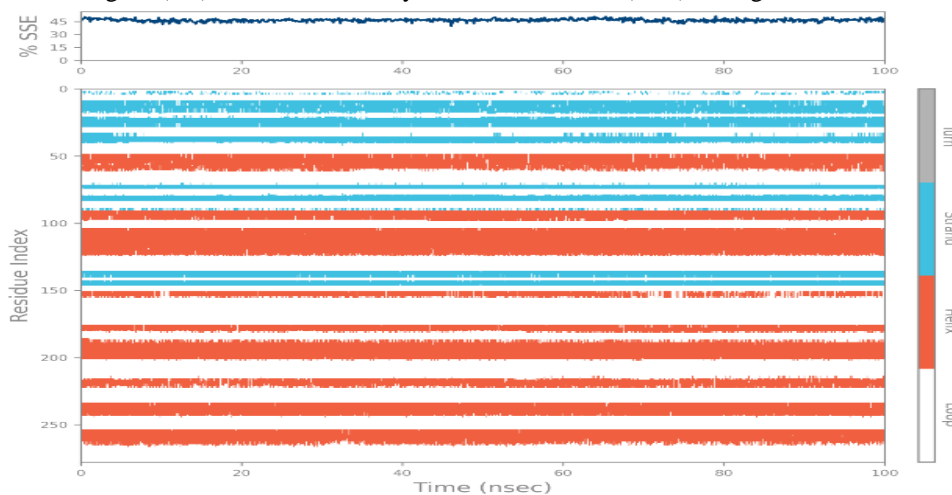


Figure (7B): Protein secondary structure elements (SSE) during simulation.

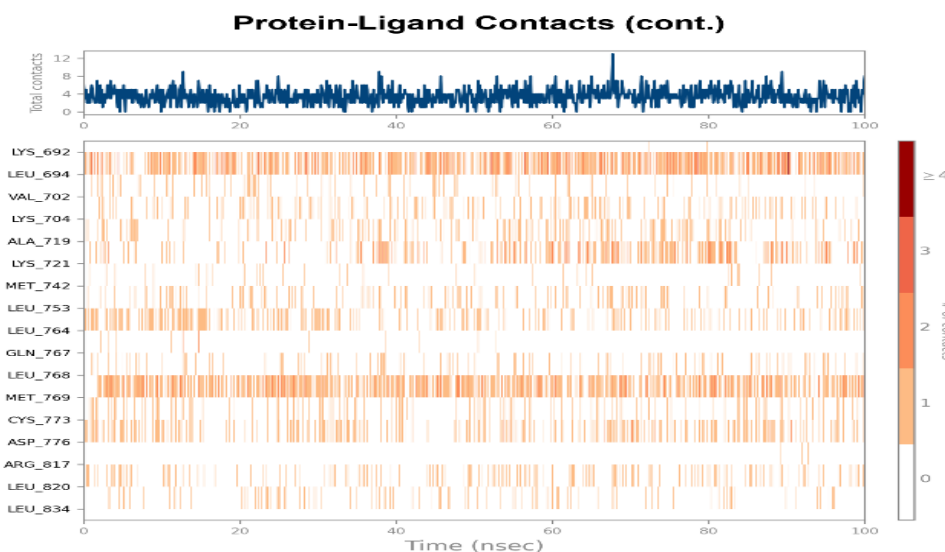


Figure (8): Protein-ligand interactions of amino acids with Compound A1 during the Simulation period.

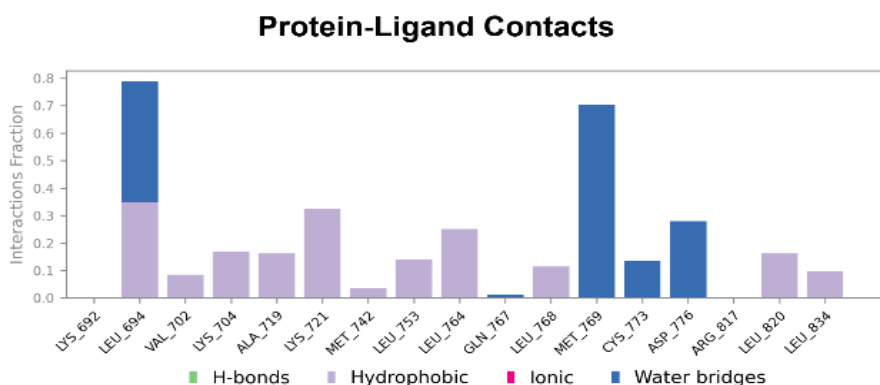


Figure (9): Protein-ligand contact histogram showing the type of bond forming with the amino acid within the active site.

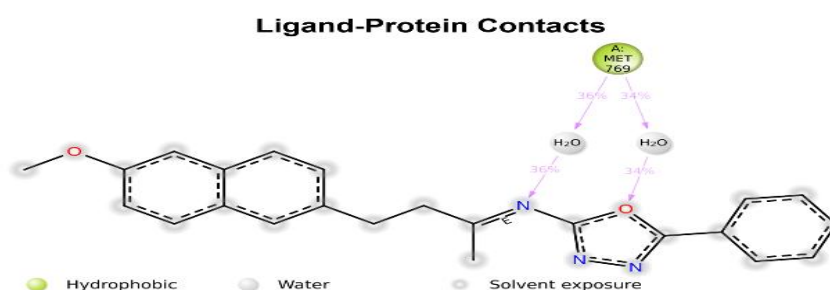


Figure (10): Ligand- Protein Contacts showing the ligand interaction and bond formation present during simulation.

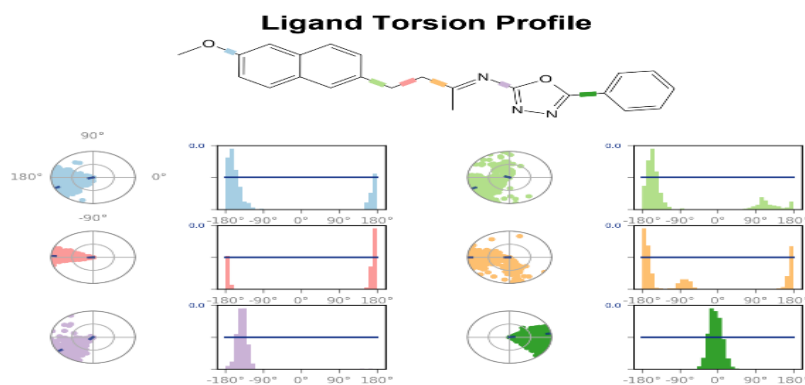


Figure (11): Ligand Torsion Profile.

Water bridges were formed and observed, accompanied by residues such as MET769, which occurred over 36% of the simulation time, as shown in Figure 10.

3.3.5 Ligand Torsion Profile

The ligand torsions plot offers a detailed view of the conformational shifts in each rotatable bond (RB) of the ligand during the simulation, which ranges from 0.00 to 100 nanoseconds. The top panel

displays a 2D image of the ligand, featuring color-coded rotatable bonds for ease of understanding. The torsion of each rotatable bond is illustrated using a dial plot, paired with a matching bar plot in the same color. These dial plots effectively visualize the torsional changes over time. The analysis of rotatable bonds in A1 showed minimal torsional strain during the simulation. The stable torsional angles indicate that A1 maintained

an energetically favorable conformation, contributing to its strong binding affinity. The torsion profile indicates that A1 does not undergo significant structural strain to fit into the binding pocket, as illustrated in Figure 11.

4. Conclusions

In this study, we designed and screened novel 1,3,4-oxadiazole and 1,3,4-thiadiazole derivatives as potential EGFR inhibitors using molecular docking, ADMET result analysis, and molecular dynamics simulations.

Among the synthesized derivatives, compounds A1 and A2, as determined by molecular docking results, exhibited higher binding affinities compared to the reference compound, Erlotinib. These results can be explained by their strong hydrogen bonding and hydrophobic interactions. The A1 compound also presented good ADMET profiles, as most of the compounds followed Lipinski's Rule of Five and displayed good absorption, permeability, and metabolic stability. A1, A3, and A4 exhibited similar pharmacokinetic behavior to Erlotinib, whereas A2 was less permeable. The pharmacokinetics were favorable, especially in complying with Lipinski's Rule of Five.

Consistent with the MD simulations, which indicated that A1 was stable and formed reliable interactions with key residues in EGFR during various periods of the simulation trajectory, stable interaction was observed for 100 ns of the A1-EGFR complex, as indicated by RMSD, RMSF, and stable secondary structure in the protein, demonstrating the utility of A1 as a potent and selective inhibitor.

In conclusion, A1 emerged as the most promising inhibitor, exhibiting high docking affinity, a favorable ADMET profile, and stable behavior during molecular dynamics (MD) simulations. While these findings are encouraging, experimental validation will be crucial for confirming the efficacy and safety of EGFR-targeted therapies.

Acknowledgement

The authors would like to thank Mustansiriyah University (www.uomustansiriyah.edu.iq) in Baghdad, Iraq, for their support in completing this work.

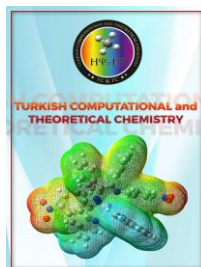
References

- [1] G. Boloker, C. Wang, J. Zhang, Updated statistics of lung and bronchus cancer in United States (2018), *J Thorac Dis* 10 (2018) 1158.
- [2] H.A. Hasan, K.F. Ali, W.A. Mehdi, Synthesis, characterization, docking study and biological activates of new 3-aminorhodanine derivatives, *Al Mustansiriyah Journal of Pharmaceutical Sciences* 24 (2024) 299-310.
- [3] T. Amelia, R.E. Kartasasmita, T. Ohwada, D.H. Tjahjono, Structural insight and development of EGFR tyrosine kinase inhibitors, *Molecules* 27 (2022) 819.
- [4] M.F. Mahdi, A.M. Raauf, Molecular modelling, synthesis and antiproliferative evaluation of new (phenyldiazenyl)-pyrazol Schiff base derivatives, *Al Mustansiriyah J Pharm Sci* 24 (2024) 25-37.
- [5] K. Bhanumathy, A. Balagopal, F.S. Vizeacoumar, F.J. Vizeacoumar, A. Freywald, V. Giambra, Protein tyrosine kinases: their roles and their targeting in leukemia, *Cancers* 13 (2021) 184.
- [6] F.A. Shepherd, J. Pereira, T.E. Ciuleanu, E.H. Tan, V. Hirsh, S. Thongprasert, A. Bezjak, D. Tu, P. Santabarbara, L. Seymour, A randomized placebo-controlled trial of erlotinib in patients with advanced non-small cell lung cancer following failure of first- or second-line chemotherapy, *J Clin Oncol* 22 (2004) 7022.
- [7] K. Park, E.H. Tan, K. O'Byrne, L. Zhang, M. Boyer, T. Mok, V. Hirsh, J.C.H. Yang, K.H. Lee, S. Lu, Y. Shi, L. Paz-Ares, Afatinib versus gefitinib as first-line treatment of patients with EGFR mutation-positive non-small-cell lung cancer (LUX-Lung 7): a phase 2B, open-label, randomised controlled trial, *Lancet Oncology* 17 (2016) 577-589.
- [8] P.A. Jänne, J.C.H. Yang, D.W. Kim, D. Planchard, Y. Ohe, S.S. Ramalingam, M.J. Ahn, S.W. Kim, W.C. Su, L. Horn, D. Häggström, AZD9291 in EGFR inhibitor-resistant non-small-cell lung cancer, *N Engl J Med* 372 (2015) 1689-1699.
- [9] Y.L. Zhang, J.Q. Yuan, K.F. Wang, X.H. Fu, X.R. Han, D. Threapleton, Z.Y. Yang, C. Mao, J.L. Tang, The prevalence of EGFR mutation in patients with non-small cell lung cancer: a systematic review and meta-analysis, *Oncotarget* 7 (2016) 78985-78993.
- [10] M. Shaikh, Y. Shinde, R. Pawara, M. Noolvi, S. Surana, I. Ahmad, H. Patel, Emerging approaches to overcome acquired drug resistance obstacles to osimertinib in

- non-small-cell lung cancer, *J Med Chem* 65 (2021) 1008-1046.
- [11] S. Abdallah, V. Hirsh, Irreversible tyrosine kinase inhibition of epidermal growth factor receptor with afatinib in EGFR activating mutation-positive advanced non-small-cell lung cancer, *Curr Oncol* 25 (2018) 9-17.
- [12] B.C. Cho, J.Y. Han, S.W. Kim, K.H. Lee, E.K. Cho, Y.G. Lee, D.W. Kim, J.H. Kim, G.W. Lee, J.S. Lee, B.Y. Shim, A phase 1/2 study of lazertinib 240 mg in patients with advanced EGFR T790M-positive NSCLC after previous EGFR tyrosine kinase inhibitors, *J Thorac Oncol* 17 (2022) 558-567.
- [13] T.S. Mok, Y.L. Wu, M.J. Ahn, M.C. Garassino, H.R. Kim, S.S. Ramalingam, F.A. Shepherd, Y. He, H. Akamatsu, W.S. Theelen, C.K. Lee, Osimertinib or platinum-pemetrexed in EGFR T790M-positive lung cancer, *N Engl J Med* 376 (2017) 629-640.
- [14] R. Roskoski Jr, Classification of small-molecule protein kinase inhibitors based upon the structures of their drug-enzyme complexes, *Pharmacol Res* 103 (2016) 26-48.
- [15] J.C. Soria, Y. Ohe, J. Vansteenkiste, T. Reungwetwattana, B. Chewaskulyong, K.H. Lee, A. Dechaphunkul, F. Imamura, N. Nogami, T. Kurata, I. Okamoto, Osimertinib in untreated EGFR-mutated advanced non-small-cell lung cancer, *N Engl J Med* 378 (2018) 113-125.
- [16] I. Ahmad, R. Pawara, A. Pathan, H. Patel, in: *Natural Products as Enzyme Inhibitors: An Industrial Perspective*, Springer Nature, Singapore, 2022, 1-23.
- [17] [Y. Jia, C.H. Yun, E. Park, D. Ercan, M. Manuia, J. Juarez, C. Xu, K. Rhee, T. Chen, H. Zhang, S. Palakurthi, Overcoming EGFR (T790M) and EGFR (C797S) resistance with mutant-selective allosteric inhibitors, *Nature* 534 (2016) 129-132.
- [18] R. Pal, G. Teli, G.S.P. Matada, P.S. Dhiwar, Designing strategies, structure-activity relationship and biological activity of recently developed nitrogen-containing heterocyclic compounds as epidermal growth factor receptor tyrosinase inhibitors, *J Mol Struct* 1291 (2023) 136021.
- [19] N.W. Ibrahim, M. Mahdi, A.M. Raauf, Design, molecular docking, synthesis and evaluation of new isatin derivatives bearing pyridine moiety as potential tyrosine kinase inhibitors, *Egypt J Chem* 65 (2022) 9-18.
- [20] B.K. Jameel, A.M. Raauf, W.A.K. Abbas, Synthesis, characterization, molecular docking, in silico ADME study and in vitro cytotoxicity evaluation of new pyridine derivatives of nabumetone, *Al Mustansiriyah J Pharm Sci* 23 (2023) 250-262.
- [21] [21] T. Glomb, K. Szymankiewicz, P. Świątek, Anti-cancer activity of derivatives of 1,3,4-oxadiazole, *Molecules* 23 (2018) 3361.
- [22] N. Kerru, L. Gummidi, S. Maddila, K.K. Gangu, S.B. Jonnalagadda, A review on recent advances in nitrogen-containing molecules and their biological applications, *Molecules* 25 (2020) 1909.
- [23] M.J. Akhtar, A.A. Siddiqui, A.A. Khan, Z. Ali, R.P. Dewangan, S. Pasha, M.S. Yar, Design, synthesis, docking and QSAR study of substituted benzimidazole linked oxadiazole as cytotoxic agents, EGFR and erbB2 receptor inhibitors, *Eur J Med Chem* 126 (2017) 853-869.
- [24] U. Bhanushali, S. Kalekar-Joshi, R. Kulkarni-Munshi, S. Yellanki, R. Medishetty, P. Kulkarni, R.S. Chelakara, Design, synthesis and evaluation of 5-pyridin-4-yl-2-thioxo-[1,3,4]oxadiazol-3-yl derivatives as anti-angiogenic agents targeting VEGFR-2, *Anti-Cancer Agents Med Chem* 17 (2017) 67-74.
- [25] S. S. Ismaeel, M.F. Mahdi, B.M. Abd Razik, Design, synthesis and antibacterial study of new agents having 4-thiazolidinone pharmacophore, *Egypt J Chem* 63 (2020) 2591-2603.
- [26] U.A. Çevik, D. Osmaniye, S. Levent, B.N. Sağlık, B.K. Çavuşoğlu, A.B. Karaduman, Y. Özkay, Z.A. Kaplancikli, Synthesis and biological evaluation of novel 1,3,4-thiadiazole derivatives as possible anticancer agents, *Acta Pharm* 70 (2020) 499-513.
- [27] S.R. Atta-Allah, A.M. Aboul Magd, P.S. Farag, Design, microwave-assisted synthesis and molecular modeling study of some new 1,3,4-thiadiazole derivatives as potent anticancer agents and potential

- VEGFR-2 inhibitors, *Bioorganic Chemistry* 112 (2021) 104923.
- [28] C.E. Stecoza, G.M. Nitulescu, C. Drăghici, M.T. Caproiu, A. Hanganu, O.T. Olaru, D.P. Mihai, M. Bostan, M. Mihăilă, Synthesis of 1,3,4-thiadiazole derivatives and their anticancer evaluation, *Int J Mol Sci* 24 (2023) 17476.
- [29] B. Shaker, S. Ahmad, J. Lee, C. Jung, D. Na, In silico methods and tools for drug discovery, *Comput Biol Med* 137 (2021) 104851.
- [30] F. Stanzione, I. Giangreco, J.C. Cole, in: D.R. Witty, B. Cox (Eds.), *Progress in medicinal chemistry* 60 2021, 273-343.
- [31] I.A. Guedes, C.S. de Magalhães, L.E. Dardenne, Receptor-ligand molecular docking, *Biophysical reviews* 6 (2014) 75-87.
- [32] M.S. Badar, S. Shamsi, J. Ahmed, M.A. Alam, in: *Transdisciplinarity*, Springer International Publishing, Cham, 2022, 131-151.
- [33] F. Wu, Y. Zhou, L. Li, X. Shen, G. Chen, X. Wang, X. Liang, M. Tan, Z. Huang, Computational approaches in preclinical studies on drug discovery and development, *Front Chem* 8 (2020) 726.
- [34] M. Amer, M.F. Mahdi, A.K. Khan, A.M. Raauf, Design, molecular docking, synthesis, preliminary in silico ADME studies and anti-inflammatory evaluation of new oxazole derivatives, *J Pharm Negat Results* 13 (2022) 217-228.
- [35] M.L. Verdonk, V. Berdini, M.J. Hartshorn, W.T.M. Mooij, C.W. Murray, R.D. Taylor, P. Watson, Virtual screening using protein-ligand docking: avoiding artificial enrichment, *J Chem Inf Comput Sci* 44 (2004) 793-806.
- [36] Y.A.F. Ghazi, M.F. Mahdi, A.H. Dawood, Theoretical drug design, molecular docking and ADME study of new 1,3,4-oxadiazole derivatives: promising anticancer agents against both breast and lung cancers, *Egypt J Chem* 64 (2021) 6269-6283.
- [37] A.K. Wabdan, M.F. Mahdi, A.K. Khan, Molecular docking, synthesis and ADME studies of new pyrazoline derivatives as potential anticancer agents, *Egypt J Chem* 64 (2021) 4311-4322.
- [38] J. Delhommelle, D.J. Evans, Comparison of thermostating mechanisms in NVT and NPT simulations of decane under shear, *J Chem Phys* 115 (2001) 43-49.
- [39] C.A. Lipinski, Lead- and drug-like compounds: the rule-of-five revolution, *Drug Discov Today: Technol* 1 (2004) 337-341.
- [40] T.S. Carpenter, D.A. Kirshner, E.Y. Lau, S.E. Wong, J.P. Nilmeier, F.C. Lightstone, A method to predict blood-brain barrier permeability of drug-like compounds using molecular dynamics simulations, *Biophys J* 107 (2014) 630-641.
- [41] J.S. Bhardwaj, S. Manandhar, S. Chatterjee, G. Hari, K. Priya, S. Raviteja, K.S.R. Pai, Protective effects of gossypin in colchicine-induced cognitive dysfunction and oxidative damage in rats, *Research Journal of Pharmacy and Technology* 13 (2020) 5189-5196
- [42] D. Asano, H. Takakusa, D. Nakai, Oral absorption of middle-to-large molecules and its improvement, with a focus on new modality drugs, *Pharmaceutics* 16 (2023) 47.
- [43] G.S. Coombs, R.C. Bergstrom, J.L. Pellequer, S.I. Baker, M. Navre, M.M. Smith, J.A. Tainer, E.L. Madison, D.R. Corey, Substrate specificity of prostate-specific antigen, *Chem Biol* 5 (1998) 475-488.
- [44] R.B. Van Breemen, Y. Li, Caco-2 cell permeability assays to measure drug absorption, *Expert Opin. Drug Metab. Toxicol.* 1 (2005) 175-185.
- [45] D.A. Volpe, Drug-permeability and transporter assays in Caco-2 and MDCK cell lines, *Future Med. Chem.* 3 (2011) 2063-2077.
- [46] J.D. Irvine, L. Takahashi, K. Lockhart, J. Cheong, J.W. Tolan, H.E. Selick, J.R. Grove, MDCK (Madin-Darby canine kidney) cells: a tool for membrane permeability screening, *J Pharm Sci* 88 (1999) 28-33.
- [47] A. Cavalli, E. Poluzzi, F. De Ponti, M. Recanatini, Toward a pharmacophore for drugs inducing the long QT syndrome: insights from a CoMFA study of HERG K⁺ channel blockers, *J Med Chem* 45 (2002) 3844-3853.

- [48] [E.A. Sobh, M.A. Dahab, E.B. Elkaeed, A.A. Alsfook, I.M. Ibrahim, A.M. Metwaly, I.H. Eissa, Design, synthesis, docking, molecular dynamics simulations and anti-proliferative evaluation of thieno[2,3-d]pyrimidine derivatives as new EGFR inhibitors, *J Enzyme Inhib Med Chem* 38 (2023) 2220579.
- [49] H. Yang, Z. Zhang, Q. Liu, J. Yu, C. Liu, W. Lu, Identification of dual-target inhibitors for epidermal growth factor receptor and AKT: virtual screening based on structure and molecular dynamics study, *Molecules* 28 (2023) 7607.
- [50] V. Unadkat, S. Rohit, P. Parikh, V. Sanna, S. Singh, Rational design-aided discovery of novel 1,2,4-oxadiazole derivatives as potential EGFR inhibitors, *Bioorg Chem* 114 (2021) 105124.
- [51] M. Rahimi, M. Taghdir, F. Abasi Joozdani, Dynamozones are the most obvious sign of the evolution of conformational dynamics in HIV-1 protease, *Sci Rep* 13 (2023) 14179..



Received: 10.01.2025

Turkish Computational and Theoretical Chemistry

Turkish Comp Theo Chem (TC&TC)

Volume(Issue): 10(1) – Year: 2026 – Pages: 110-130

e-ISSN: 2602-3237

<https://doi.org/10.33435/tcandtc.1617260>

Accepted: 13.04.2025



Research Article

Supplymantery data

Simulation Interactions Diagram Report

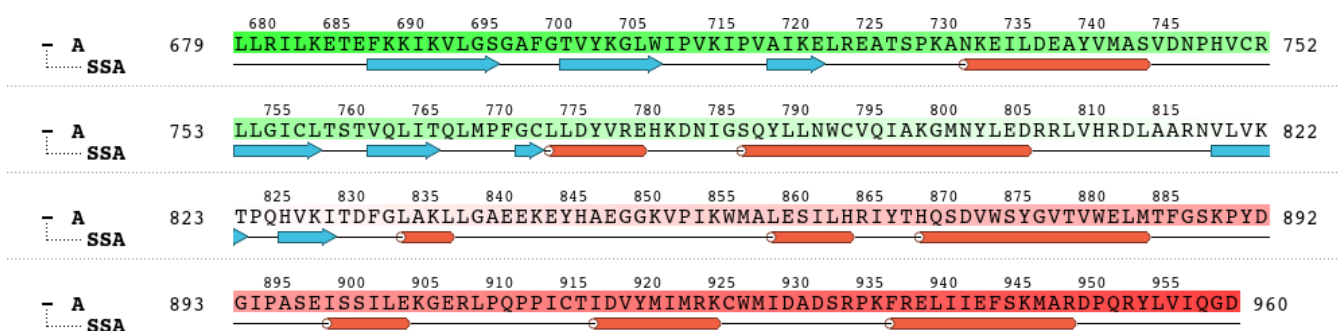
Simulation Details

Jobname: haloob-desmond_md_job_1
Entry title: 4hjo - minimized Structure1

CPU #	Job Type	Ensemble	Temp. [K]	Sim. Time [ns]	# Atoms	# Waters	Charge
1	mdsim	NPT	300.0	100.102	34019	9792	0

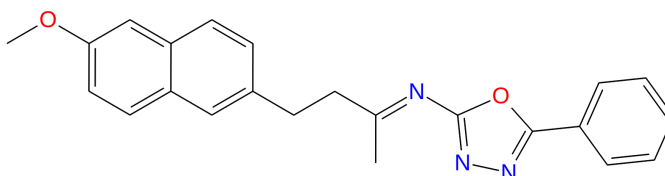
Protein Information

Tot. Residues	Prot. Chain(s)	Res. in Chain(s)	# Atoms	# Heavy Atoms	Charge
278	'A'	ict_values([278])	4535	2232	+5



Ligand Information

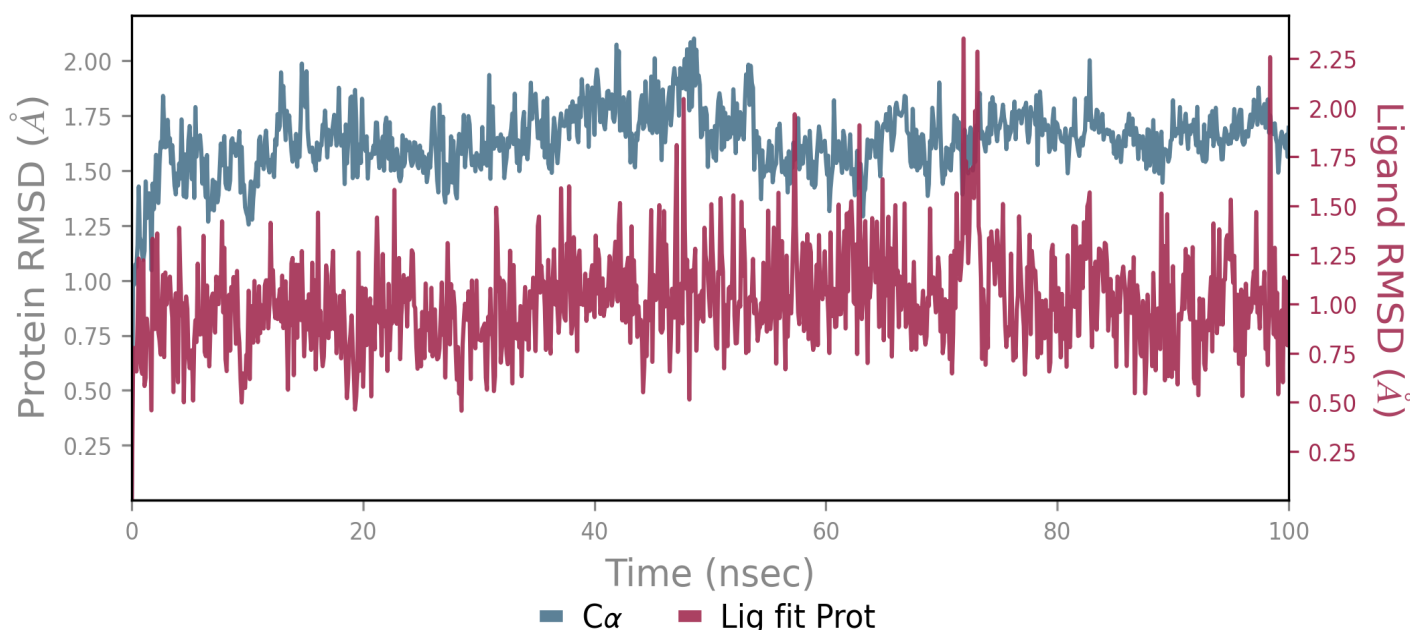
SMILES	COc(cc1)cc(c12)ccc(c2)CC/C(C)=N/c(o3)nnc3-c4ccccc4
PDB Name	'UNK'
Num. of Atoms	49 (total) 28 (heavy)
Atomic Mass	371.443 au
Charge	0
Mol. Formula	C23H21N3O2
Num. of Fragments	2
Num. of Rot. Bonds	6



Counter Ion/Salt Information

Type	Num.	Concentration [mM]	Total Charge
Cl	32	59.418	-32
Na	27	50.134	+27

Protein-Ligand RMSD



The Root Mean Square Deviation (RMSD) is used to measure the average change in displacement of a selection of atoms for a particular frame with respect to a reference frame. It is calculated for all frames in the trajectory. The RMSD for frame x is:

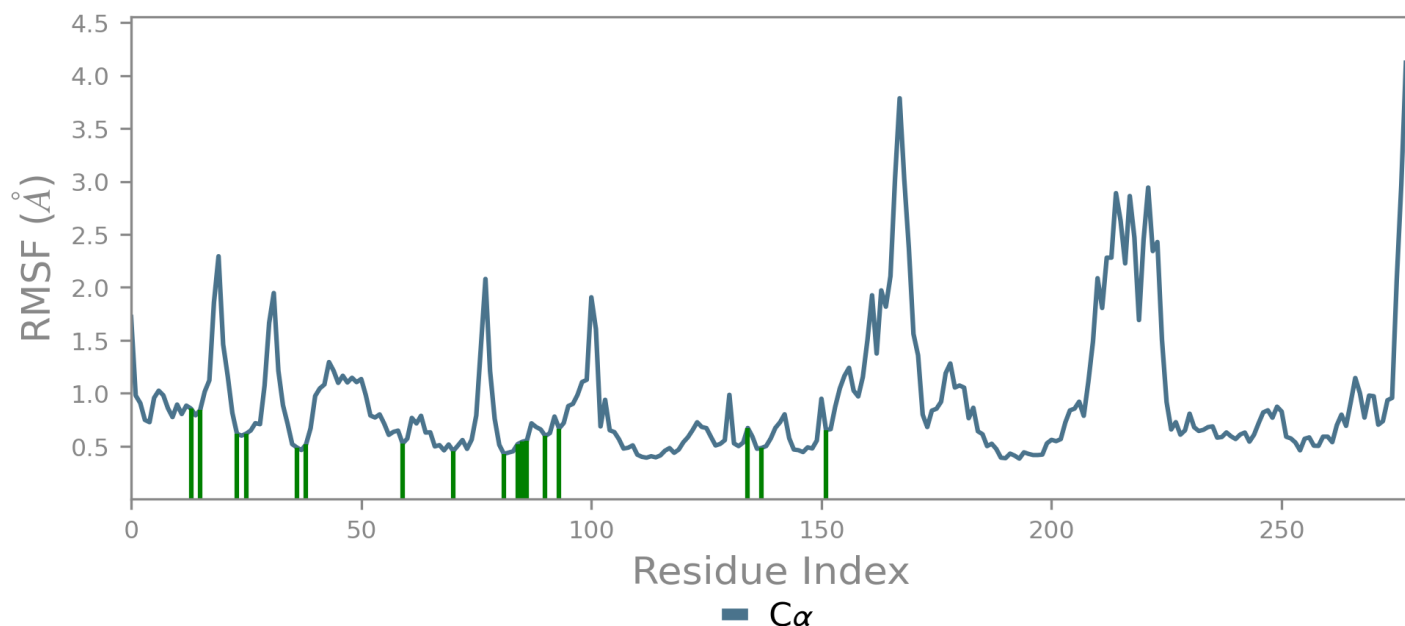
$$RMSD_x = \sqrt{\frac{1}{N} \sum_{i=1}^N (r'_i(t_x) - r_i(t_{ref}))^2}$$

where N is the number of atoms in the atom selection; t_{ref} is the reference time, (typically the first frame is used as the reference and it is regarded as time $t=0$); and r' is the position of the selected atoms in frame x after superimposing on the reference trajectory, where frame x is recorded at time t_x . The procedure is repeated for every frame in the simulation trajectory.

Protein RMSD: The above plot shows the RMSD evolution of a protein (left Y-axis). All protein frames are first aligned on the reference frame backbone, and then the RMSD is calculated based on the atom selection. Monitoring the RMSD of the protein can give insights into its structural conformation throughout the simulation. RMSD analysis can indicate if the simulation has equilibrated — its fluctuations towards the end of the simulation are around some thermal average structure. Changes of the order of 1-3 Å are perfectly acceptable for small, globular proteins. Changes much larger than that, however, indicate that the protein is undergoing a large conformational change during the simulation. It is also important that your simulation converges — the RMSD values stabilize around a fixed value. If the RMSD of the protein is still increasing or decreasing on average at the end of the simulation, then your system has not equilibrated, and your simulation may not be long enough for rigorous analysis.

Ligand RMSD: Ligand RMSD (right Y-axis) indicates how stable the ligand is with respect to the protein and its binding pocket. In the above plot, 'Lig fit Prot' shows the RMSD of a ligand when the protein-ligand complex is first aligned on the protein backbone of the reference and then the RMSD of the ligand heavy atoms is measured. If the values observed are significantly larger than the RMSD of the protein, then it is likely that the ligand has diffused away from its initial binding site.

Protein RMSF



The Root Mean Square Fluctuation (RMSF) is useful for characterizing local changes along the protein chain. The RMSF for residue i is:

$$RMSF_i = \sqrt{\frac{1}{T} \sum_{t=1}^T \langle (r'_i(t)) - r_i(t_{ref}) \rangle^2}$$

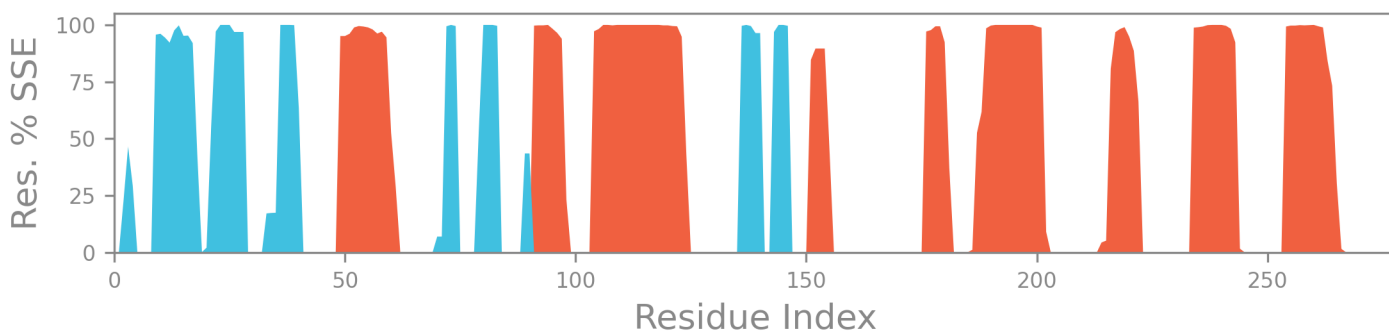
where T is the trajectory time over which the RMSF is calculated, t_{ref} is the reference time, r_i is the position of residue i ; r' is the position of atoms in residue i after superposition on the reference, and the angle brackets indicate that the average of the square distance is taken over the selection of atoms in the residue.

On this plot, peaks indicate areas of the protein that fluctuate the most during the simulation. Typically you will observe that the tails (N - and C -terminal) fluctuate more than any other part of the protein. Secondary structure elements like alpha helices and beta strands are usually more rigid than the unstructured part of the protein, and thus fluctuate less than the loop regions.

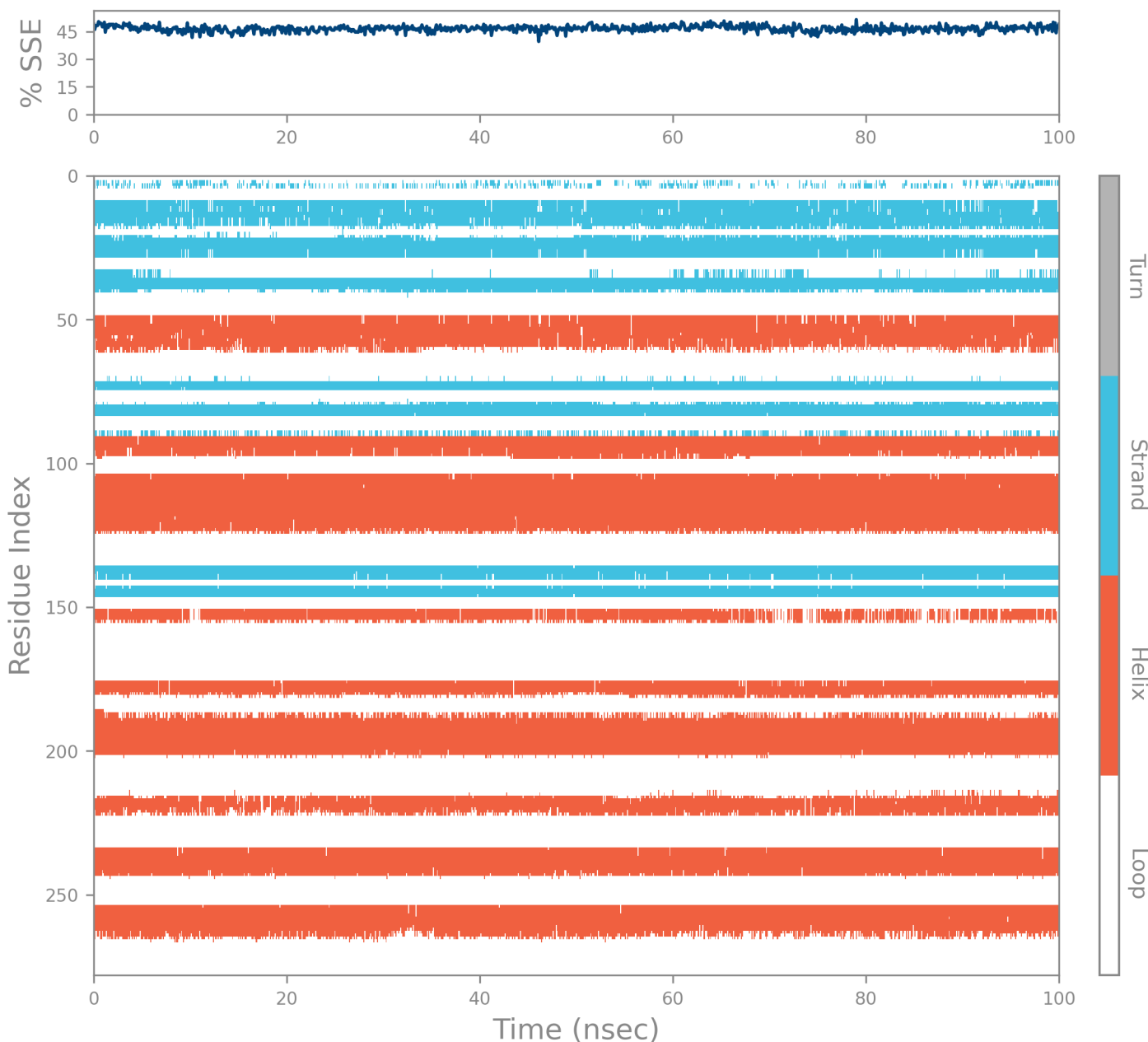
Ligand Contacts: Protein residues that interact with the ligand are marked with green-colored vertical bars.

Protein Secondary Structure

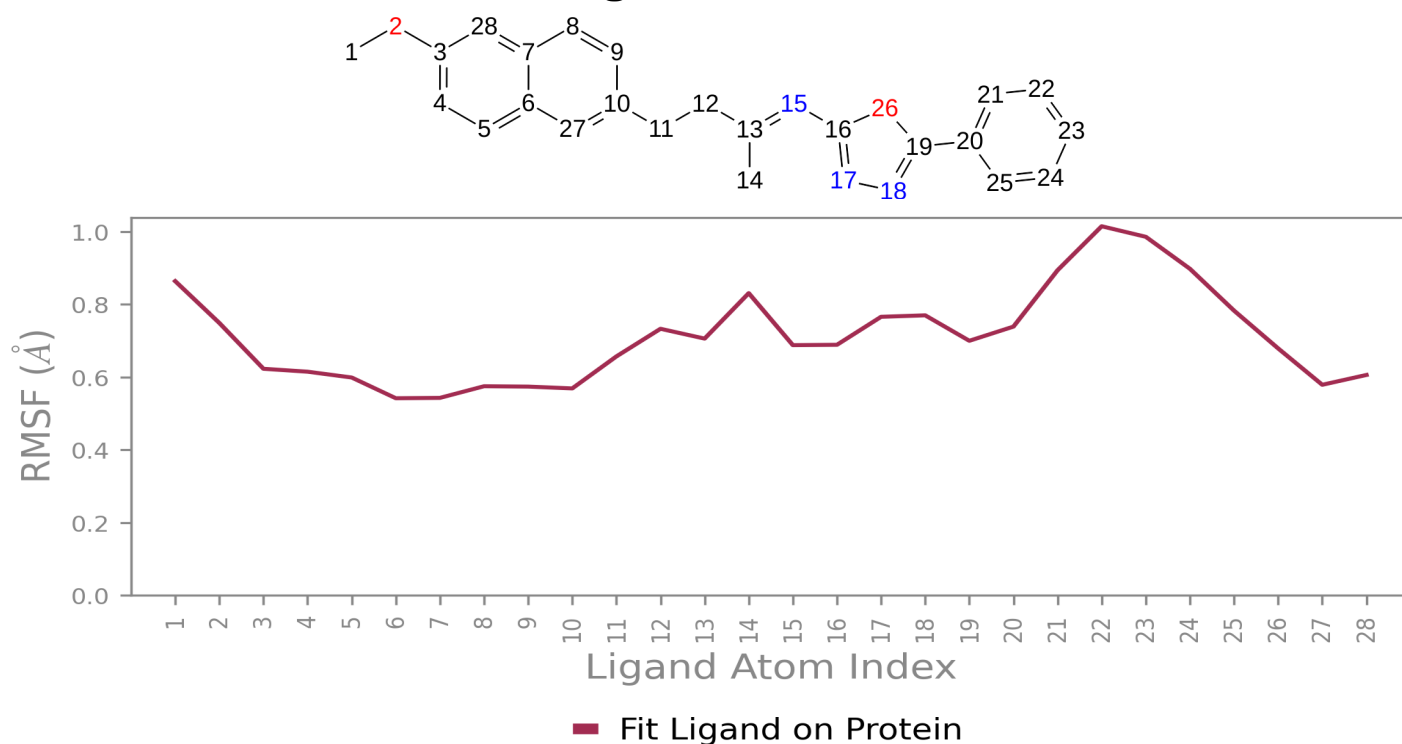
% Helix	% Strand	% Total SSE
32.18	14.39	46.56



Protein secondary structure elements (SSE) like **alpha-helices** and **beta-strands** are monitored throughout the simulation. The plot above reports SSE distribution by residue index throughout the protein structure. The plot below summarizes the SSE composition for each trajectory frame over the course of the simulation, and the plot at the bottom monitors each residue and its SSE assignment over time.



Ligand RMSF



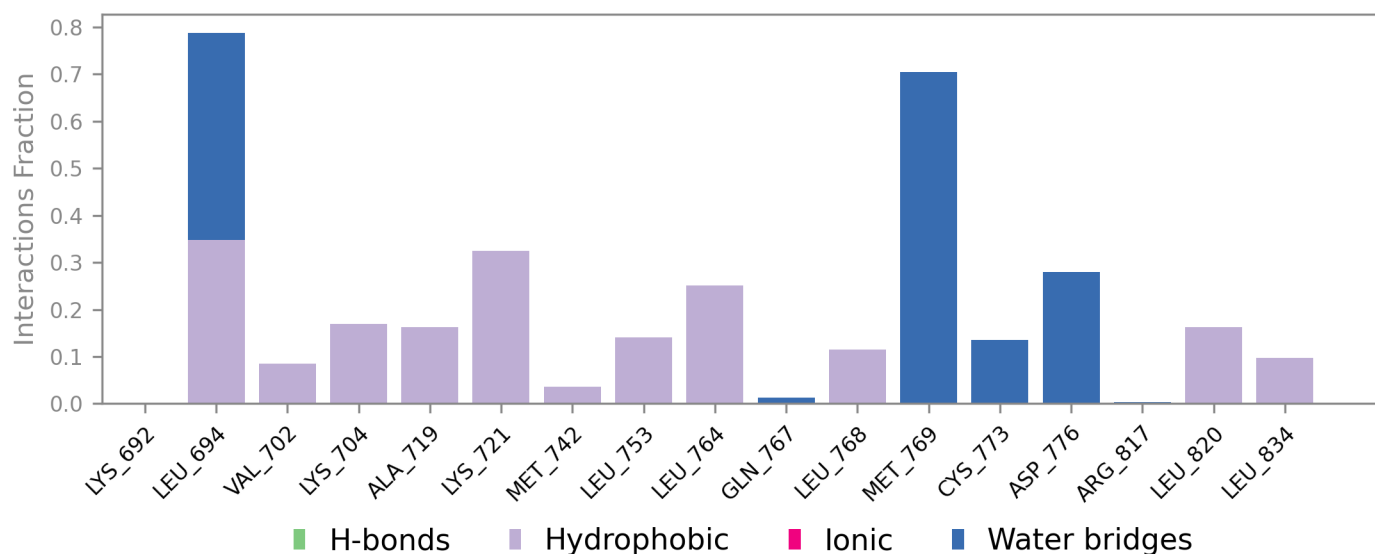
The Ligand Root Mean Square Fluctuation (L-RMSF) is useful for characterizing changes in the ligand atom positions. The RMSF for atom i is:

$$RMSF_i = \sqrt{\frac{1}{T} \sum_{t=1}^T (r'_i(t) - r_i(t_{ref}))^2}$$

where T is the trajectory time over which the RMSF is calculated, t_{ref} is the reference time (usually for the first frame, and is regarded as the zero of time); r is the position of atom i in the reference at time t_{ref} and r' is the position of atom i at time t after superposition on the reference frame.

Ligand RMSF shows the ligand's fluctuations broken down by atom, corresponding to the 2D structure in the top panel. The ligand RMSF may give you insights on how ligand fragments interact with the protein and their entropic role in the binding event. In the bottom panel, the 'Fit Ligand on Protein' line shows the ligand fluctuations, with respect to the protein. The protein-ligand complex is first aligned on the protein backbone and then the ligand RMSF is measured on the ligand heavy atoms.

Protein-Ligand Contacts



Protein interactions with the ligand can be monitored throughout the simulation. These interactions can be categorized by type and summarized, as shown in the plot above. Protein-ligand interactions (or 'contacts') are categorized into four types: Hydrogen Bonds, Hydrophobic, Ionic and Water Bridges. Each interaction type contains more specific subtypes, which can be explored through the 'Simulation Interactions Diagram' panel. The stacked bar charts are normalized over the course of the trajectory: for example, a value of 0.7 suggests that 70% of the simulation time the specific interaction is maintained. Values over 1.0 are possible as some protein residue may make multiple contacts of same subtype with the ligand.

Hydrogen Bonds: (H-bonds) play a significant role in ligand binding. Consideration of hydrogen-bonding properties in drug design is important because of their strong influence on drug specificity, metabolism and adsorption. Hydrogen bonds between a protein and a ligand can be further broken down into four subtypes: backbone acceptor; backbone donor; side-chain acceptor; side-chain donor.

The current geometric criteria for protein-ligand H-bond is: distance of 2.5 Å between the donor and acceptor atoms (D—H...A); a donor angle of $\geq 120^\circ$ between the donor-hydrogen-acceptor atoms (D—H...A); and an acceptor angle of $\geq 90^\circ$ between the hydrogen-acceptor-bonded_atom atoms (H...A—X).

Hydrophobic contacts: fall into three subtypes: π -Cation; π - π ; and Other, non-specific interactions. Generally these type of interactions involve a hydrophobic amino acid and an aromatic or aliphatic group on the ligand, but we have extended this category to also include π -Cation interactions.

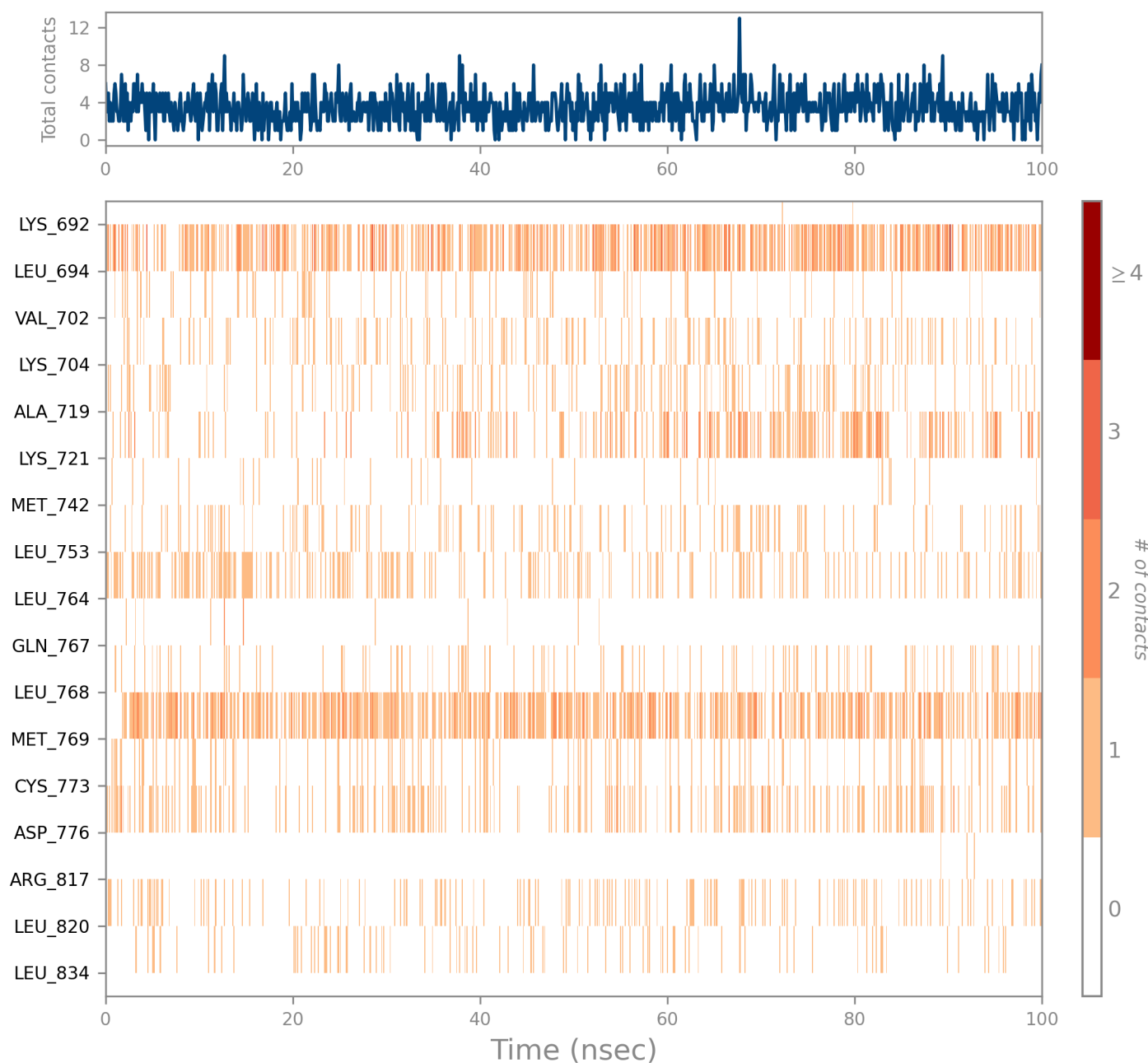
The current geometric criteria for hydrophobic interactions is as follows: π -Cation — Aromatic and charged groups within 4.5 Å; π - π — Two aromatic groups stacked face-to-face or face-to-edge; Other — A non-specific hydrophobic sidechain within 3.6 Å of a ligand's aromatic or aliphatic carbons.

Ionic interactions: or polar interactions, are between two oppositely charged atoms that are within 3.7 Å of each other and do not involve a hydrogen bond. We also monitor Protein-Metal-Ligand interactions, which are defined by a metal ion coordinated within 3.4 Å of protein's and ligand's heavy atoms (except carbon). All ionic interactions are broken down into two subtypes: those mediated by a protein backbone or side chains.

Water Bridges: are hydrogen-bonded protein-ligand interactions mediated by a water molecule. The hydrogen-bond geometry is slightly relaxed from the standard H-bond definition.

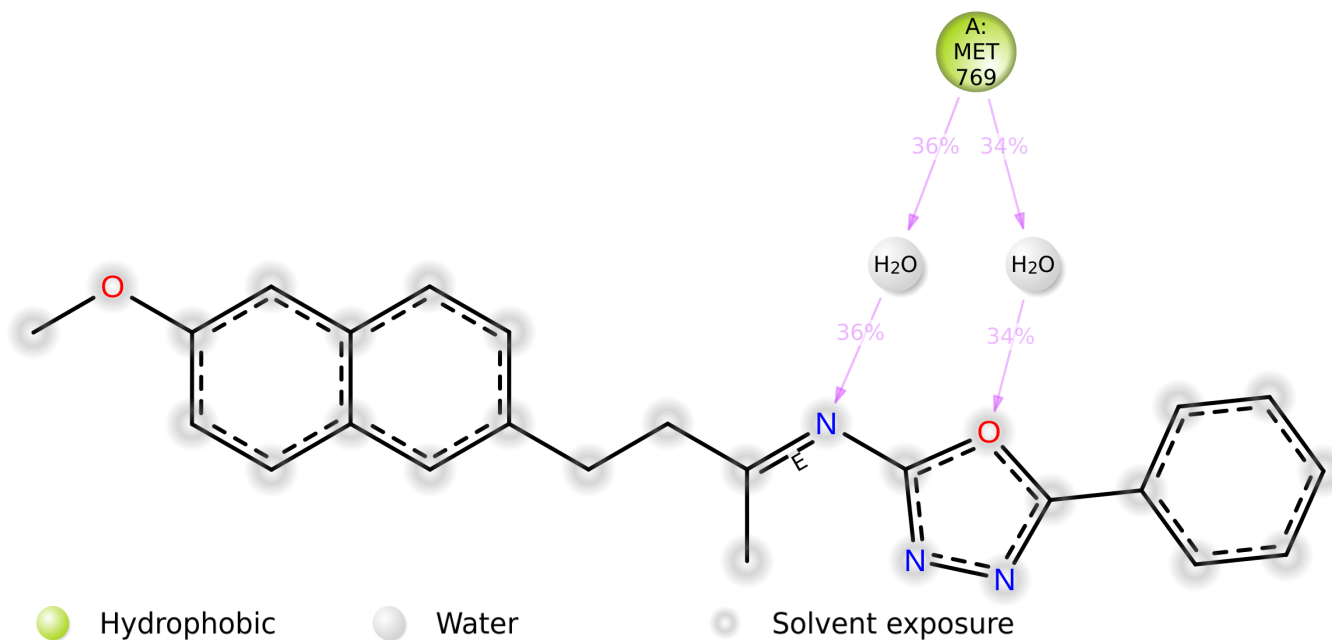
The current geometric criteria for a protein-water or water-ligand H-bond are: a distance of 2.8 Å between the donor and acceptor atoms (D—H...A); a donor angle of $\geq 110^\circ$ between the donor-hydrogen-acceptor atoms (D—H...A); and an acceptor angle of $\geq 90^\circ$ between the hydrogen-acceptor-bonded_atom atoms (H...A—X).

Protein-Ligand Contacts (cont.)



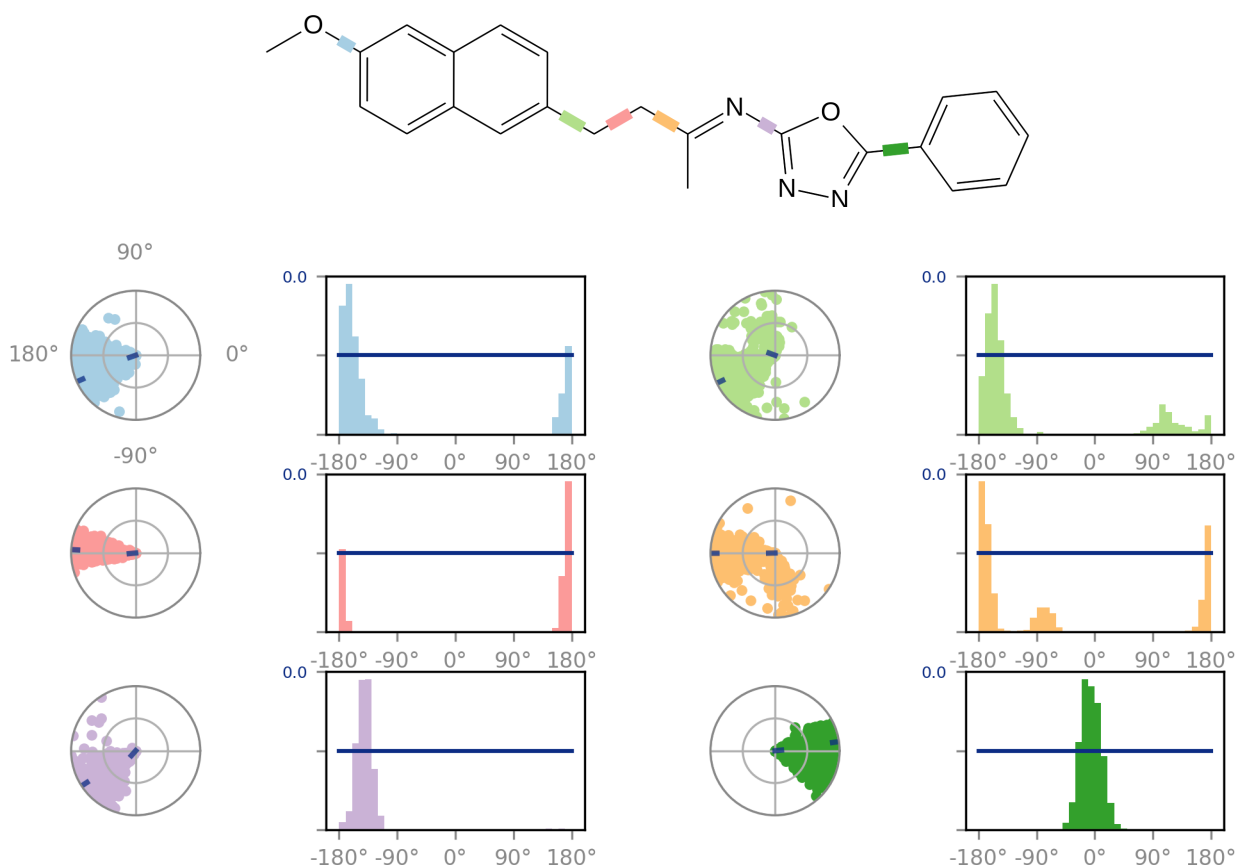
A timeline representation of the interactions and contacts (**H-bonds, Hydrophobic, Ionic, Water bridges**) summarized in the previous page. The top panel shows the total number of specific contacts the protein makes with the ligand over the course of the trajectory. The bottom panel shows which residues interact with the ligand in each trajectory frame. Some residues make more than one specific contact with the ligand, which is represented by a darker shade of orange, according to the scale to the right of the plot.

Ligand-Protein Contacts



A schematic of detailed ligand atom interactions with the protein residues. Interactions that occur more than **30.0%** of the simulation time in the selected trajectory (0.00 through 100.00 nsec), are shown. Note: it is possible to have interactions with >100% as some residues may have multiple interactions of a single type with the same ligand atom. For example, the ARG side chain has four H-bond donors that can all hydrogen-bond to a single H-bond acceptor.

Ligand Torsion Profile

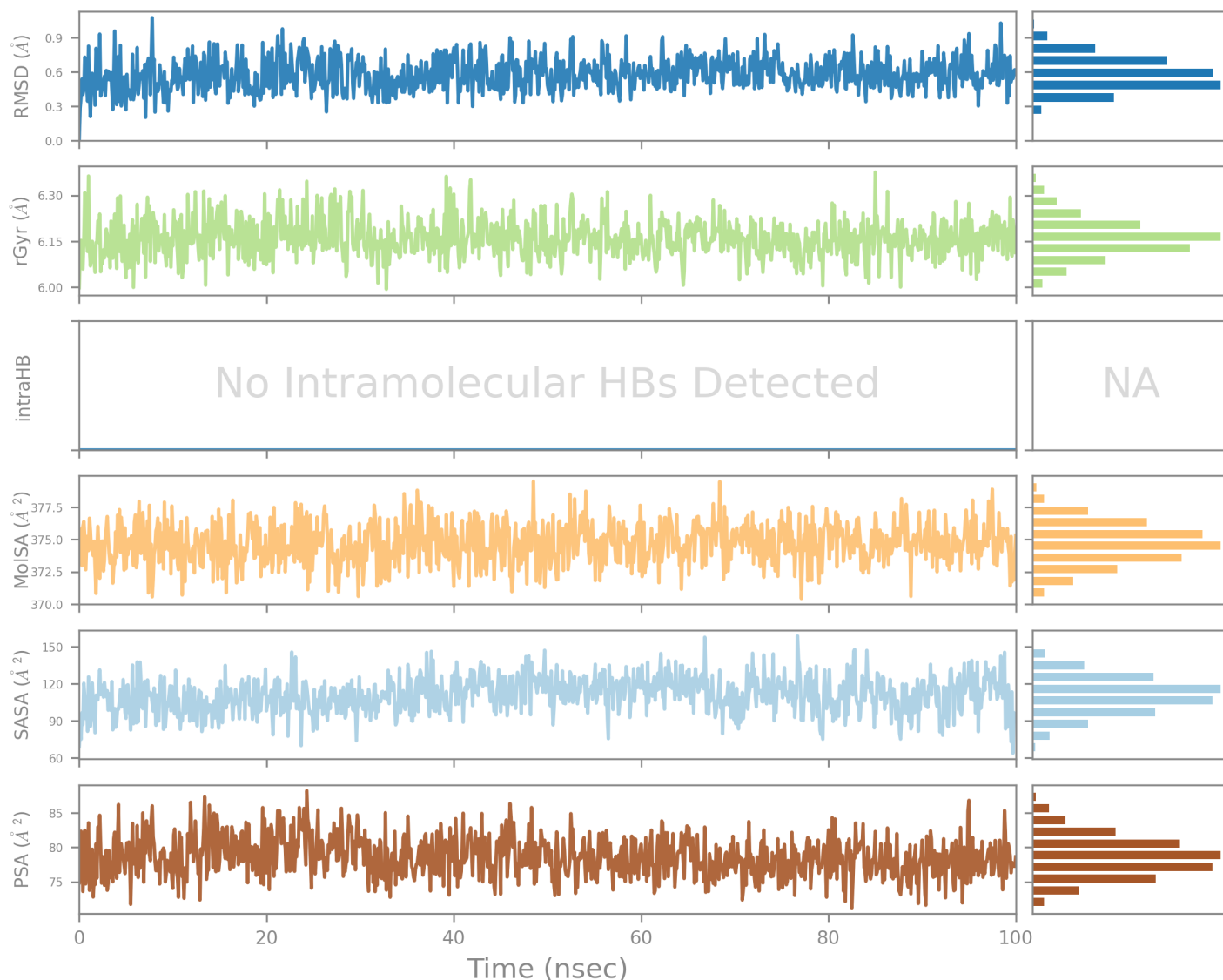


The ligand torsions plot summarizes the conformational evolution of every rotatable bond (RB) in the ligand throughout the simulation trajectory (0.00 through 100.00 nsec). The top panel shows the 2d schematic of a ligand with color-coded rotatable bonds. Each rotatable bond torsion is accompanied by a dial plot and bar plots of the same color.

Dial (or radial) plots describe the conformation of the torsion throughout the course of the simulation. The beginning of the simulation is in the center of the radial plot and the time evolution is plotted radially outwards.

The bar plots summarize the data on the dial plots, by showing the probability density of the torsion. If torsional potential information is available, the plot also shows the potential of the rotatable bond (by summing the potential of the related torsions). The values of the potential are on the left Y-axis of the chart, and are expressed in *kcal/mol*. Looking at the histogram and torsion potential relationships may give insights into the conformational strain the ligand undergoes to maintain a protein-bound conformation.

Ligand Properties



Ligand RMSD: Root mean square deviation of a ligand with respect to the reference conformation (typically the first frame is used as the reference and it is regarded as time $t=0$).

Radius of Gyration (rGyr): Measures the 'extendedness' of a ligand, and is equivalent to its principal moment of inertia.

Intramolecular Hydrogen Bonds (intraHB): Number of internal hydrogen bonds (HB) within a ligand molecule.

Molecular Surface Area (MolISA): Molecular surface calculation with 1.4 Å probe radius. This value is equivalent to a van der Waals surface area.

Solvent Accessible Surface Area (SASA): Surface area of a molecule accessible by a water molecule.

Polar Surface Area (PSA): Solvent accessible surface area in a molecule contributed only by oxygen and nitrogen atoms.